This is to certify that the
thesis entitled

CHARACTERIZATION OF A SHEAR LAYER THROUGH
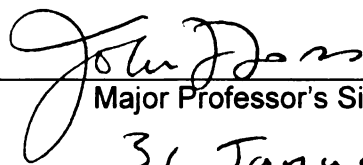PARTICLE IMAGE VELOCIMETRY

presented by

Kyle McHugh Bade

has been accepted towards fulfillment
of the requirements for the

__Master of Science__   degree in   __Mechanical Engineering__

_____
Major Professor's Signature

31 January 2007
Date

PLACE IN RETURN BOX to remove this checkout from your record.
TO AVOID FINES return on or before date due.
MAY BE RECALLED with earlier due date if requested.

DATE DUE	DATE DUE	DATE DUE

CHARACTERIZATION OF A SHEAR LAYER THROUGH

PARTICLE IMAGE VELOCIMETRY

By

Kyle McHugh Bade

A THESIS

Submitted to
Michigan State University
in partial fulfillment of the requirements
for the degree of

MASTER OF SCIENCE

Department of Mechanical Engineering

2007

ABSTRACT

CHARACTERIZATION OF A SHEAR LAYER THROUGH PARTICLE IMAGE VELOCIMETRY

By

Kyle M. Bade

An experimental investigation of a shear layer using particle image velocimetry (PIV) to acquire instantaneous realizations of the flow field was conducted. Detailed PIV data were acquired across the primary flow inlet region as well as over a large downstream domain. The instantaneous flow field observations were used to create ensemble flow field statistics. The initial momentum thickness was $\theta_o = 1.11$mm. The mean inlet velocity of the primary flow was $\overline{U}_{o,x=0} = 4.51$m/s. The Reynolds number, based on these scales, was $Re_{\theta_o} = 321$. Boundary layer results nominally agreed with the Blasius solution at x=0.

The experimental facility's spatial constraints created a large scale recirculating flow. The primary flow velocity was $\overline{U}_o = 4.6$m/s in the downstream data region: $495 < x/\theta_o < 567$. The growth rate of the downstream shear layer, within the range of $\overline{u}/\overline{U}_o = 0.13$ to 1.0, was $d\theta/dx = 0.032$. This growth rate is indicative of a single stream shear layer.

A topological 'collapsed sphere' surface was used to analyze across the single-stream shear layer region over the downstream range noted above. Singular points (nodes and saddles) were identified in the instantaneous velocity fields. Large scale coherent motions were identified in a convection speed reference frame. The subset of these motions, which could be fully characterized, exhibited the following quantities: i) mean location of a coherent motion center: $\overline{u}/\overline{U}_o = 0.66$ isotach, ii) size of the average motion $\left(\langle \frac{L}{\theta(x)} \rangle = 3.34 \right)$ where L^2 is the area bounded by the circulation contour, iii) strength of the spatially averaged motion $\left(\langle \frac{\overline{\omega}_z \theta(518\theta_o)}{\overline{U}_o} \rangle = -20.4 \right)$.

ACKNOWLEDGEMENTS

TABLE OF CONTENTS

LIST OF TABLES

LIST OF FIGURES

NOMENCLATURE

Roman:

A	Circulation Contour Area
$d_{N/S}$	Distance from a Node to the Associated Saddle
dt	Image Frame-Pair Time Delay
$\vec{D}$	Distance Traveled of Particles in PIV Correlation Window
I(0,1)	Intermittency Function
L	Length of One Side of a Square Circulation Contour
n	Index of Refraction
N	Total Number of Samples (Vectors)
ΣN	Sum of Nodes
$\Sigma N'$	Sum of Half-Nodes
P_1	Primary (highest) Cross-Correlation Peak
P_2	Secondary (second highest) Cross-Correlation Peak
P_{min}	Lowest Cross-Correlation Peak Level
q	Planar Velocity Magnitude (x-y plane)
Q	PIV Vector Validation Minimum Required Peak Ratio
Re_{θ_0}	Reynolds Number based on θ_0
ΣS	Sum of Saddles
$\Sigma S'$	Sum of Half-Saddles
u	Streamwise Velocity
$\bar{u}$	Mean Streamwise Velocity
$\tilde{u}$	Streamwise Turbulence Intensity

$\overline{U}_{13}$	13% of the Maximum Mean Streamwise Velocity
U_c	Mean Streamwise Convection Velocity
$\overline{U}_{o,x=0}$	Maximum Mean Streamwise Velocity at the Backstep
$\overline{U}_o$	Maximum Mean Streamwise Velocity Downstream
v	Spanwise Velocity
$\vec{V}$	Velocity Vector of Particles in PIV Correlation Window
x	Streamwise Coordinate
y	Spanwise Coordinate
y_c	Distance from a Node Center to the $(0.5)\overline{U}_o$ Mean Isotach
$y_{1/2}$	Spanwise Location where $\overline{u} = (\overline{U}_o)/2$
z	Out-of-Plane Coordinate

Greek:

$\dfrac{d\theta}{dx}$	Shear Layer Growth Rate
η	Normalized Spanwise Coordinate
$\theta_{13}(x)$	Momentum Thickness at a given Streamwise Location (x), from $\overline{U}_{13}$ to $\overline{U}_o$
θ_o	Initial Momentum Thickness
$\theta(x)$	Momentum Thickness at a given Streamwise Location (x)
$\chi_{surface}$	Surface Euler Characteristic
$\vec{\Gamma}$	Circulation
$\vec{\omega}$	Vorticity
$\omega_z(t)$	Time variant vorticity in the z-direction

Acronyms:

CCD	Charge Coupled Device
DEHS	Bis(2-ethylhexyl) Sebdecate
LHS	Left Hand Side
Nd:YAG	Neodymium-doped Yttrium Aluminium Garnet; Nd:Y3Al5O12
PIV	Particle Image Velocimetry
PTU	Programmable Timing Unit
RHS	Right Hand Side
RMS	Root mean square
SSSL	Single-Stream Shear Layer
TSFL	Turbulent Shear Flows Laboratory

Facility and Equipment Components (chapters 2 and 3 only):

[A]	Flow Inlet Portal
[B]	Flow Outlet Portal
[C]	Primary Blower
[D]	Lower Plenum
[E]	Receiver Plenum
[F]	Test-Section Opening
[G]	Lower Plenum Static Pressure Tap
[H]	Receiver Plenum Static Pressure Tap
[I]	Inlet Flow Baffles
[J]	Inlet Flow Re-Entry Channels

[K]	Steel Test-Section Mounting Brackets
[L]	Support Frame
[M]	Support Frame Holes
[N]	Test-Section Support Board
[O]	Test-Section Support Board Holes for Threaded Positioning Rods
[P]	Threaded Positioning Rods
[Q]	Laser Head x2
[R]	Laser Control Boxes x2
[S]	PIV Computer and PTU
[T]	PIV CCD Camera
[U]	Aspirator (PIV Flow Seeder)
[V]	Modular Focusing Lens for the Laser Beam
[W]	Differential Pressure Transducer
[X]	Divergent Lens for the Laser Sheet
[Y]	Laser Cooling Lines
[Z]	Focusing Lens for the Camera
[AA]	Light Filter for the Camera
[BB]	PIV Calibration Plate

1.0 Introduction

1.1 Initial Motivation

The focus of this experimental investigation is to identify the physical phenomena on the low speed side of a single-stream shear layer (SSSL). Specifically, the motivation for this work was to acquire and analyze detailed PIV data across the superlayer of the entrainment side flow and to use these data to characterize the intermittency region. Over the course of these experiments many experimental techniques were used in evaluating test setups and facility components including pressure measurements, hotwire measurements, and PIV measurements. The primary data analyzed herein are derived from PIV observations across the subject shear layer.

The majority of tests and time was spent in the large single stream shear layer located in the Turbulent Shear Flows Lab (TSFL) at Michigan State University. This facility was originally constructed in 1999 by Scott C. Morris with the help of co-workers. Dr. Morris conducted his Ph.D. research in the facility under the direction of Dr. John Foss. The primary focus of those experiments was the transition region from a turbulent boundary layer to a single-stream shear layer (Morris (2002) and Morris & Foss (2003)). This unique SSSL facility has the attractive quality of possessing very large initial length scales; the initial momentum thickness (θ_0) at separation, for example, was 9.6mm with a Reynolds number based on this initial momentum thickness of $Re_{\theta_0} = 4650$.

Following the efforts by Dr. Morris in the large SSSL, an extensive hotwire investigation of the intermittency region on the high-speed side of the downstream shear layer was carried out by Aren Hellum (Hellum (2006)). Hellum defined the intermittency function ($I = 0,1$) on the basis of $\omega_z(t)$. A threshold and a dwell time were required for this

I=0,1 discrimination. This hot-wire investigation worked quite well in this region given the strong streamwise component of the velocity field.

The logical focus for the next effort in the coordinated research effort of this single stream shear layer, was an investigation of the low speed side entrainment region of the SSSL. The proposed method for this investigation was to utilize PIV techniques which would allow the intermittency region to be studied despite the large fluctuations in flow direction and superlayer location that are experienced in this region. However, in practice this proved to be quite difficult to accomplish without disrupting the non-vortical entrainment fluid. This difficulty was primarily due to the need to introduce seed particles into the system in order to acquire PIV images. The large SSSL facility employs a driven low speed side flow which is calibrated to deliver the appropriate mass flow of entrained fluid to the low speed side of shear layer (see Morris & Foss (2003)). The low speed side entrainment flow is driven with four large, low pressure rise fans which are upstream of a series of flow conditioning elements. This setup allows the majority of the driven entrainment flow to escape upstream of the flow conditioners. By allowing a substantial portion of this driven flow to escape, the low speed flow is provided to the shear layer, but is not forced into the shear layer. Seed particles could not be distributed upstream of the flow conditioners without clogging the conditioning screens, increasing the restriction, and altering the entrainment flow calibration. Additionally, the majority of the seed would not be present in the test-section. Distribution of the seed particles downstream of the flow conditioners without disrupting the low speed side entrainment flow could not be accomplished for this work.

In addition to the low speed side entrainment flow seeding issues, the primary flow is quite difficult to adequately seed due to large out-of-plane diffusion of the seeding fluid prior to it reaching the downstream region of interest.

After extensive efforts to overcome the seeding difficulties, a more suitable PIV facility was employed to complete this investigation. The efforts and results of the investigations in the large SSSL are discussed further in Appendix A of this thesis. The new facility is described in detail in chapter 2.

1.2 Motivation (for Present Experiments)

A single-stream shear layer test-section was built to allow for a PIV investigation of a shear layer using the PIV facility. A uniform seed was achieved in all regions of the shear layer test-section by utilizing the PIV facility. The PIV facility and the constructed single stream shear layer test-section are discussed in great detail in chapters 2 and 3 respectively. The primary focus of the present investigation remains the low speed entrainment side of the single-stream shear layer and the associated intermittency region. After acquiring, processing, and investigating 1000 PIV images, extensive work was completed to characterize the flow field, and specifically, the low speed side of the shear layer. The investigations were ultimately based upon topological considerations that are further identified in section 1.4.

1.3 Shear Layer Mechanics

The dynamics of a single-stream shear layer are driven by a primary flow. The resulting interaction of this primary flow with the entrained fluid creates the shear layer which grows in the spanwise direction as the fluid convects downstream. Figure 1.1 dem-

onstrates the most notable components of a single-stream shear layer. The primary flow, which is directly driven by the blower, provides a nearly uniform streamwise (+x) velocity flow. When this flow reaches the backstep, it is suddenly and immediately bordered by the un-forced low speed side entrainment flow. Once the primary flow encounters the back-step, the interaction of these two flows results in the formation of the shear layer region. For a comprehensive description of the entrainment and vorticity induction of low speed side fluid see Dimotakis (1986).

1.4 Topology of a Velocity Field

Topological analysis allows for the investigation of a continuous vector field with an a-priori knowledge of the net basic flow structures based on the flow field geometry. Analysis of a flow field geometry provides a surface Euler Characteristic ($\chi_{surface}$). This constraint must also be satisfied by the net flow structures on that surface. A topological surface may exist on a physical surface or within the flow field. For the investigations provided here, a topological sphere (or single deformable volume) will be collapsed in depth to the mid-plane (x,y,z=0) of the test-section. The velocity field vectors will exist on the internal surface of this 'collapsed sphere'. Therefore, three holes allow the primary and entrained flows to pass through the collapsed sphere and exit downstream. Some basic topological descriptions are discussed here, for a more complete discussion, Foss (2004) and Perry & Chong (1987) are recommended. For the purposes of these experiments it will only be necessary to investigate a collapsed sphere surface and this collapsed sphere will exist at the centerplane of the SSSL test-section.

1.4.1 Collapsed Sphere Topology

The accounting of singular points provides insight into the flow structures based on the surrounding geometry. The first step is to determine the geometry-based Euler Characteristic defined by:

$$\chi_{surface} = 2 - 2\Sigma handles - \Sigma holes. \tag{1.1}$$

Following the determination of this Euler Characteristic, the flow structures (singular points), contained within the topological sphere, must agree with the Euler Characteristic. Nodes and saddles may also exist as half-nodes and half-saddles on a collapsed sphere surface. The topological accounting of singular points is demonstrated in equation 1.2.

$$\chi_{surface} = 2\Sigma N + \Sigma N' - 2\Sigma S - \Sigma S' \tag{1.2}$$

By first determining the Euler Characteristic based on the geometry (which provides the topological constraint), the investigator is able to determine the proper number of *net* nodes, half-nodes, saddles, and half-saddles. Using this Euler Characteristic, a flow which is compatible with the determined Euler Characteristic constraint can be determined. This method can be employed for an instantaneous flow image as well as for an averaged situation, however, an instantaneous flow field can be much more complex. The instantaneous flow field will, however, still arrive at the same net singular point accounting and Euler Characteristic.

1.4.2 SSSL Collapsed Sphere Geometry and Accounting

The topological assessment of this SSSL setup provides clear insight into the ensemble average flow structure. As seen in Figure 1.2, there are three holes and no handles for this geometry.

$$\chi_{surface} = 2 - 2\Sigma handles - \Sigma holes = 2 - 2(0) - 3 = -1 \tag{1.3}$$

The surface in this setup is chosen so that the primary inlet and the low speed side entrained flow both approach their respective in-flow holes uniformly, also, the downstream exit flow exits uniformly to its hole. The seams are chosen to be parallel with the flow along strategic streamlines, seams connect holes and allow no flow to pass through them. The obvious locations for this flow field are the sidewall and the backstep wall. The third seam follows a streamline which, on average, the flow moves downstream without crossing.

The only singular point to be inferred from this geometry comes immediately at the backstep and is a half-saddle,

$$\chi_{surface} = 2\Sigma N + \Sigma N' - 2\Sigma S - \Sigma S' = 0 + 0 - 0 - 1 = -1 \qquad (1.4)$$

this is demonstrated in Figure 1.2. Therefore, the total Euler Characteristic is $\chi_{surface} = -1$ based on both the geometry and the mean flow field singular point investigations. With an educated assessment of the overall mean flow structure, detailed measurements can now be carried out on the flow field and analyzed with a preconceived mean flow solution and a known net topology.

Mean Shear Layer Region

Streamline

Entrained Flow

Backstep

Primary Flow
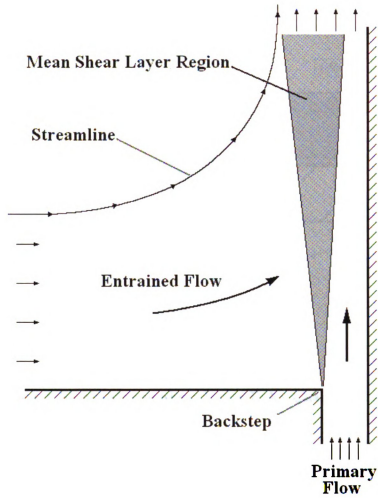
Figure 1.1 Single-Stream Shear Layer Flow Model
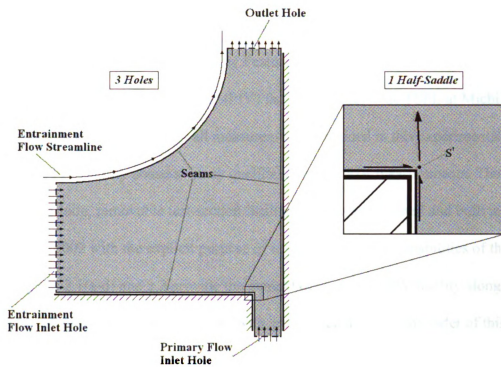
Figure 1.2 Single-Stream Shear Layer Euler Characteristic

2.0 PIV Facility and Test-Section

2.1 General Overview of the PIV Facility

2.1.1 PIV Facility Specifications and Key Features

The Particle Image Velocimetry (PIV) facility located in the TSFL at Michigan State University was employed for all measurements contained in this experimental investigation. The PIV facility possess' many qualities ideal for PIV measurements. The facility is a closed-loop, removable test-section facility which was designed and built in December of 2002 with the explicit purpose of improving the PIV capabilities of the TSFL. Figures 2.1(a-d) and 2.2 provide the general design of the PIV facility along with labeled key elements which are described with greater detail in the remainder of this chapter.

2.1.1.1 Closed-Loop Test Facility

A closed-loop flow testing system provides an ideal situation for many PIV experiments. By employing a closed-loop flow system, the seed (or particulate) material required for PIV measurements is recirculated through the flow system. The flow inlet[A] and outlet portals[B] to the PIV facility are labeled in Figure 2.1. Careful consideration was taken in positioning the outlet portal as far away as possible from the test section, as well as conditioning the flow as it returns to the test-section portion of the PIV facility. Baffles[I] are located just past where the flow re-enters the PIV facility lower section. These baffles, along with the re-entry channels[J], help to more evenly distribute the flow across the entire lower plenum[D].

The primary benefit of employing a closed-loop flow system, for these experiments, was the ability to seed both the primary and entrained flows with a single seeding

system. By recirculating the seeded flow through the flow system, a nearly steady-state level of seed was achieved throughout the entire flow system. This made it possible to achieve not only uniform seeding in each stream, but the same level of seeding in both the primary and entrained streams. Achieving this balance can be difficult in multi-stream flows.

A secondary benefit of the closed-loop flow system used here was the conservation of the seeding particulate. Over the course of these experiments, testing time for a single data set ranged from a few minutes to nearly an hour. By initially filling the system to the proper density of seed and then greatly reducing the seeding rate, very little seed was added continuously once the proper seed density was achieved. It is assumed that the lowered level of seeding rate used approximately one-quarter the seeding material as the initial rate.

2.1.1.2 Non-Reflective Surfaces

All surfaces inside the PIV facility are painted to minimize all laser light reflections. All surfaces have a two-layered coating to maximize absorption of light, especially light which is of the wavelength emitted from the PIV lasers. The undercoat is a flat-black paint, the overcoat is a rhodamine 6G dye and water mixture. The flat-black undercoat pre-darkens the surfaces which reduces reflections of all light. The overcoat of rhodamine 6G dye maximizes the absorbtion of light of the wavelength emitted by the lasers. Absorbing laser light before it reflects greatly reduces any chance of secondary or tertiary image planes that can occur with bright reflections. By eliminating the possibility of any intense reflections, the illuminated seed particles are dominantly those within the primary image plane.

A second desirable property of rhodamine 6G is a high resistance to photobleaching by light with high intensity such as that used in PIV. By covering all permanent surfaces inside the PIV facility with rhodamine 6G, the PIV facility itself is protected from the intense PIV laser light. The laser light would eventually burn through the flat-black underlayer and expose more reflective material without this protective outer coating.

2.1.1.3 Removable Test-Section

The PIV facility is built with an open-section with mounting brackets which are used to secure the test-section in place between the lower and receiving plenums, this opening is labeled in Figure 2.2 as element [F]. This generic test-section opening allows for many possible experimental test-sections to be installed. The mounting portion of the test-section opening is constructed with steel angle brackets which are welded together at the corners for added structural strength. The steel mounting brackets[K] have a 5mm thick layer of foam weather stripping which is compressed when the test-section is installed, this ensures there will be no flow leakage across this interface. The test section is held in place with 16 mounting bolts which run through the installed test-section and thread into the steel supports at approximately 18cm intervals on all four sides of the test-section. The test-section constructed for these experiments is further discussed in section 2.2.

2.1.2 Blower Specifications

The primary flow in these experiments was driven by a single blower[C] located outside of the PIV facility, its location can be seen in Figure 2.1. This blower was a Cincinnati centrifugal blower with radial blades (zero blade curvature). The blower's rotor

diameter was ~48cm and its exit portal was ~11.5cm in diameter. The driving motor was fully powered for all experiments and the limiting gate was in the fully-open position. Figure 2.3 provides a photo of the blower connected to the PIV facility system. It is worth noting that the blower was positioned on its side, relative to its support base, in order to properly orient the inlet and outlet of the blower with the PIV facility flow plumbing. During operation the pressure rise from the PIV facility lower plenum[D] to the receiver plenum[E] was monitored via static pressure taps at locations [G] and [H] respectively. The pressure drop across this interface was monitored during all tests using a pressure transducer located inside the PIV Facility. The pressure level was observed to remain very regular throughout each test and from one test to the next.

2.2 Shear Layer Test-Section Fabrication and Segment Specifics

The test-section fabricated for these experiments consisted of multiple segments which were assembled in place with the test-section opening of the PIV facility. The single-stream shear layer that was created was meant to provide an idealized setup for PIV measurements with uniform seeding throughout the test section.

2.2.1 Test-Section segments

The test-section was constructed in 4 segments which were pre-assembled into 2 sub-assemblies. These 2 sub-assemblies were then aligned and mounted to the PIV facility test-section opening. Figure 2.4 provides a two-dimensional profile view of the test-section. Each of the four segments is described in more detail in the following sections.

2.2.1.1 Inlet Segment

12

The inlet segment is the first portion of the test-section the flow encounters as it leaves the lower plenum. Figure 2.6 shows the uninstalled inlet segment, also, Figure 2.4 provides a profile view of the inlet segment. This segment provides a smooth transition from the lower plenum to the downstream segments. This segment consisted of a rounded inlet and a contraction, see Figure 2.4. The key dimensions of this segment can be seen in Figure 2.5. The lower edge of the rounded inlet was located approximately 50cm from the lower plenum floor to allow for uniform, unobstructed flow entry. Immediately following the rounded inlet was a smooth contraction to accelerate the flow and decrease the flow channel area, this contraction was gradual to ensure that the flow remained attached to the channel walls.

2.2.1.2 Flow Conditioning Segment

Once the flow has been reduced to the proper dimensions it is conditioned to have nominally uniform streamwise velocity and minimal disturbances. This segment consisted of a straight channel with a combination of screens and honeycomb. The screens create a restriction which causes a pressure drop across each screen which aides in evenly distributing the flow velocity across the entire channel area. The initial screen also serves to support the honeycomb material. The screens also provide a uniform small scale disturbance that can help to breakdown larger scale vortical motions and provide a disturbed, but uniformly disturbed, flow field. The honeycomb material is one-inch in depth and prohibits any motions of a larger length scale than the diameter of each individual cell from exiting the honeycomb. These cells were one-eighth of an inch wide in this case. Figure 2.4 demonstrates the locations of screens and honeycomb, a photograph of the inlet segment as well as the flow conditioning segment is provided as Figure 2.6. This segment provides a

nearly uniform velocity, uniform small-scale disturbance flow field to the backstep region segment.

2.2.1.3 Backstep Region Segment

The purpose of these experimental data is to investigate a single-stream shear layer and to examine the resulting low speed side entrainment region/shear layer interaction. This situation is created by constructing a four-walled channel with one of the walls making a sharp perpendicular bend in the spanwise direction, often referred to as a backstep. The resulting primary flow entrains fluid from the backstep opening and a single stream shear layer is created. Figure 2.4 provides a planar representation of this setup. The primary flow opening (+y) in this case was 10cm wide and the depth (+/-z) of the section was 50cm. The data collected here were acquired at the centerline of the testing-section (z=0), 25cm from the front and back walls. The smooth backstep extends 30cm in the spanwise (-y) direction. The PIV facility wall, in the negative y-direction, is 119cm from the backstep location. There are multiple small steps as well as the PIV laser tripod legs between end of the smooth backstep region and the PIV facility walls. The backstep itself is located 15cm downstream of the final flow conditioning screen, see Figure 2.5 for clarification of these dimensions.

Construction of the backstep region was done primarily with flat-black foamboard. This material is 5mm thick and provided a light-weight, sturdy frame for the walls of the backstep region. The entire front of the test-section was a single sheet of one-eighth inch thick glass chosen to assist in obtaining an undistorted PIV image. By utilizing a very thin, high quality sheet of glass, distortions due to refraction of light inside of the glass medium was virtually eliminated. Refraction can be a serious problem in image acquisi-

tion across multiple mediums with different indices of refraction (n). For an example of refraction distortion see Figure 2.7. The light traveling to the camera has very little (negligible in this case) distance over which to refract. The glass wall extends for 5cm below the backstep (-x) in order to allow for an inlet flow investigation of the boundary layer, via PIV.

2.2.1.4 Downstream Shear Layer Segment

The downstream region (+x) where the primary data were collected was constructed of the same materials as the backstep region. These two regions were constructed from material that reached from upstream of the backstep to the furthest downstream region in order to ensure the transition from the backstep to the downstream shear layer was as smooth as possible. This downstream region extends 81cm downstream of the initial backstep, the primary PIV data were acquired from approximately 43.5cm to 73.5cm downstream. Beyond the end of the downstream region there is no interference until the flow reaches the PIV facility ceiling, this occurs at 131cm downstream of the backstep. Figure 2.5 provides these dimensions concerning the test-section's location and orientation within the PIV facility.

2.2.1.5 Final Test-Section Assembly

The final assembly of the Inlet/Flow-Conditioning segments (inlet sub-assembly) and the Backstep/Downstream segments (backstep sub-assembly) was done inside the PIV facility. This was done for two reasons; i) the fully assembled test-section could not physically fit into the PIV facility and, ii) by assembling the two sub-assemblies in-place it

was possible to assure proper support and alignment of the inlet sub-assembly which was located entirely within the lower plenum.

The assembly process was mildly complicated but allowed for careful alignment of the two sub-assemblies in only a few steps. Initially the inlet assembly was placed on the floor in the lower plenum, notice the threaded positioning rods[P] which are attached to the inlet segment in Figure 2.8. Next the backstep sub-assembly was placed onto the PIV facility steel test-section mounting brackets[K] and the positioning rods were slipped through carefully placed holes[O] in the test-section support board[N]. The support frame[L] for the inlet sub-assembly was then positioned over the backstep sub-assembly. The need for this support frame was due to the light-weight and somewhat fragile nature of the backstep sub-assembly and the weight (~40 lbs.) of the inlet sub-assembly. Once the support frame was in place, the positioning rods were placed through holes[M] in the support frame and nuts were threaded onto the positioning rods. As these nuts were tightened they slowly drew the inlet sub-assembly up off the floor of the lower plenum and towards the backstep sub-assembly. The nuts on all four rods located at the four corners of the inlet segment were tightened until the two sub-assemblies met and compressed the foam weather stripping which was placed on the top edge of the inlet sub-assembly. Fine adjustments were then made to assure that the two sub-assemblies were firmly connected and properly aligned. Figure 2.4 demonstrates the fully assembled, installed test-section in the PIV facility, and Figure 2.8 provides an actual photo of the installed test-section in the PIV facility.

a) PIV Facility Front View

Legend:
A. Flow Inlet Portal
B. Flow Outlet Portal
C. Blower
D. Lower Plenum
E. Receiver Plenum
F. Test-Section Opening
G. Pressure Tap (Lower Plenum)
H. Pressure Tap (Receiver Plenum)
I. Inlet Flow Baffles
J. Re-Entry Channels
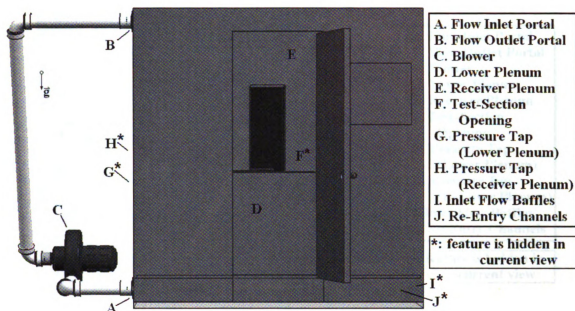
*: feature is hidden in current view
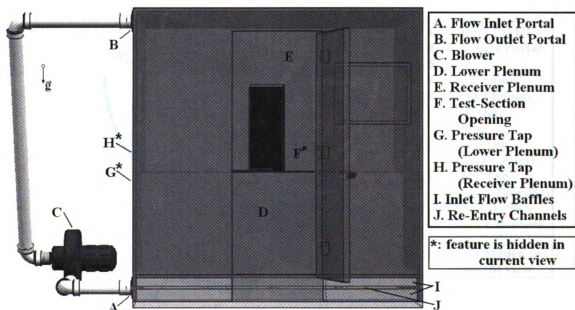
b) PIV Facility Front View (Primary Hidden Lines)

Legend:
A. Flow Inlet Portal
B. Flow Outlet Portal
C. Blower
D. Lower Plenum
E. Receiver Plenum
F. Test-Section Opening
G. Pressure Tap (Lower Plenum)
H. Pressure Tap (Receiver Plenum)
I. Inlet Flow Baffles
J. Re-Entry Channels

*: feature is hidden in current view

| A. Flow Inlet Portal |
| B. Flow Outlet Portal |
| C. Blower |
| D. Lower Plenum |
| E. Receiver Plenum |
| F. Test-Section Opening |
| G. Pressure Tap (Lower Plenum) |
| H. Pressure Tap (Receiver Plenum) |
| I. Inlet Flow Baffles |
| J. Re-Entry Channels |

*: feature is hidden in current view

c) PIV Facility Left Side View

| A. Flow Inlet Portal |
| B. Flow Outlet Portal |
| C. Blower |
| D. Lower Plenum |
| E. Receiver Plenum |
| F. Test-Section Opening |
| G. Pressure Tap (Lower Plenum) |
| H. Pressure Tap (Receiver Plenum) |
| I. Inlet Flow Baffles |
| J. Re-Entry Channels |

*: feature is hidden in current view

d) PIV Facility Bottom Angle View (Transparent Lower Floor)

Figure 2.1 PIV Facility (3D Model - 4 Perspectives)

Figure 2.2 PIV Facility 2D Model

A. Flow Inlet Portal
B. Flow Outlet Portal
C. Blower
D. Lower Plenum
E. Receiver Plenum
F. Test-Section
   Opening
G. Pressure Tap
   (Lower Plenum)
H. Pressure Tap
   (Receiver Plenum)
I. Inlet Flow Baffles
J. Re-Entry Channels
K. Mounting Brackets

*: feature is hidden in
   current view

C^* G^* H^*
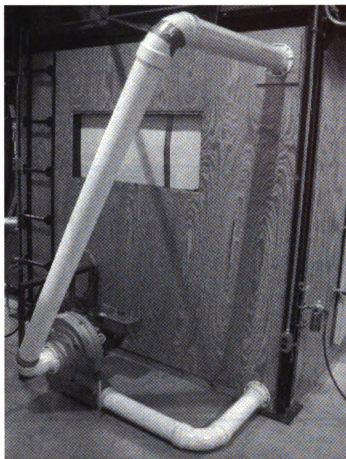
Figure 2.3 Blower & Plumbing Connected to the PIV Facility Photo

Figure 2.4 Test-Section - 2D Profile with all Segments

All Dimensions in centimeters

+x

20.5 10

50

81

Receiver Plenum
Lower Plenum

2.5

+y

15

41

43.5

74

104

6.5

63

Figure 2.5 Test-Section - Dimensioned 2D Profile
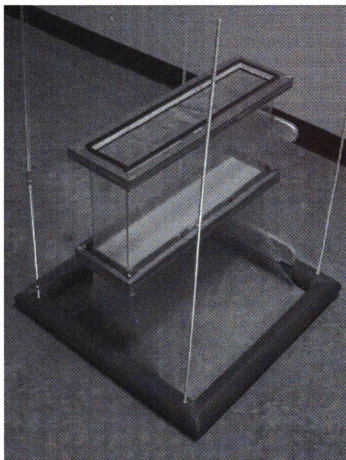
Figure 2.6 Inlet-Flow Conditioning Sub-Assembly Photo

Air   Glass   Air

| Index of Refraction: |
| Air: n≈1.0003 |
| Glass: n≈1.517 |

Beam of Light

Error due to
refraction
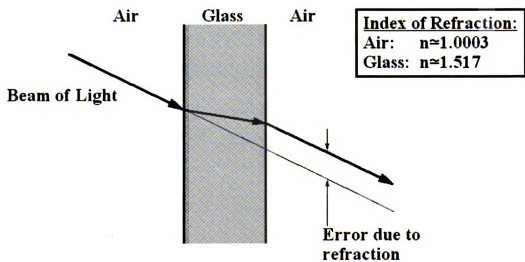
Figure 2.7 Refraction Demonstration (Air-Glass-Air)

L. Support Frame
M. Support Frame Holes
N. Test-Section Support Board
O. Support Board Holes
P. Threaded Positioning Rods
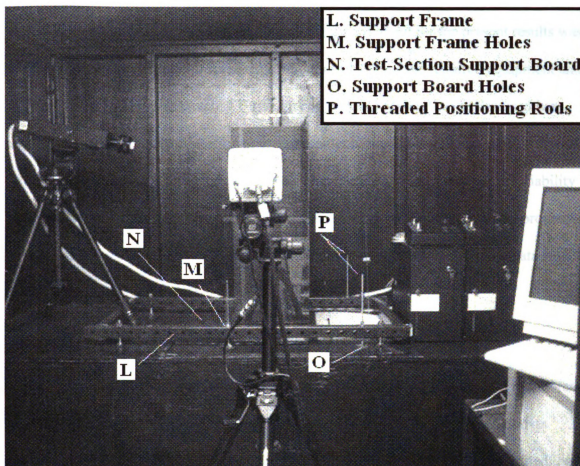
Figure 2.8 Installed Test-Section Photo

3.0   Measurement and Acquisition Equipment and Software

The data acquisition and processing that was carried out for the present results was primarily obtained through particle image velocimetry (PIV); the required equipment and software is outlined in this chapter. The main components of the PIV system used here, and in most systems, are the lasers, camera, computer with software, and a seeding device. For these measurements a pressure transducer was used to monitor and ensure reliability and repeatability of the data sets. Also, all post-processing was completed using programs written for this work in MATLAB. Visual interogation and presentation of the data was done primarily in Tecplot 360.

3.1 Pressure Transducer

The pressure drop from the lower plenum to the receiving plenum was monitored by a differential pressure transducer[W] in order to ensure that all experimental data acquisitions operated under the same conditions. This pressure differential remained very regular throughout all tests but it was a necessary check this to ensure the reliability and consistency of the system. The pressure transducer used for this purpose was a 10 torr Baratron differential pressure transducer type 398HD-00010 with a type 270B-4 signal conditioner. The accuracy of this device, as specified by MKS, was 0.05%. As previously indicated, no sampling of pressure was taken, only a 'real time check' to ensure regularity.

3.2 PIV Equipment

A LaVision PIV system was employed for these measurements. The system consists of four primary components which are i) 2 laser heads[Q] with control boxes[R], ii) a PC[S] with timing control electronics, iii) CCD camera[T] and, iv) an aspirator[U] flow

seeder. In addition to the core components just listed, there are two high-precision positioning tripods used to support and orient the lasers and camera. Each element is discussed in detail in the following sections. The positioning of each element is demonstrated in Figures 3.1 and 3.2; all main components are labeled.

3.2.1 Dual PIV Lasers

The lasers employed by the PIV system used here are New Wave Research model Minilase-III lasers. These Nd:YAG lasers emit a 1064nm wavelength (infrared) laser which is frequency-doubled to achieve a visible 532nm wavelength (green) laser beam. These lasers may operate at up to 15 Hz at 50 mJ with a pulse width of 5-7ns. The dual head design provides for a variable time between the firing of each laser which can be manually or remotely controlled. The laser heads are housed in a single assembly which orients and redirects each beam to the same point when exiting the housing. A Rodenstock modular-focusing lens[V] is mounted to the front of the dual-laser housing. This allows for focusing the laser sheet thickness and it also provides the ability to orient the diverged laser sheet to any angle. The laser sheet thickness was approximately 1mm across the image plane. The final component attached to the laser heads, mounted after the Rodenstock lens, was an interchangeable divergent lens[X] which is used to spread the laser into a sheet suitable for PIV measurements. The divergent lens used here had a focal length of 6mm which supplied a relatively large angle of divergence. The dual laser heads allowed for the acquisition of high frequency cross-correlation double-frame images.

Each laser head has an associated laser control box[R] which controls the laser firing. The control boxes can be used to control the laser pulses manually (usually for setup) or they can be connected to a PC and controlled by timing components and software. This

software is discussed further in section 3.2.3. In addition to controlling the pulsing of the lasers, the control boxes supply the cooling lines[Y] and filters for the laser heads which are cooled by recirculated deionized water.

The lasers were originally manufactured and calibrated in December of 1997 and, after many years of both heavy use and prolonged storage, the laser beams became weakened and misaligned. Prior to this research effort, both lasers were returned to New Wave and reconditioned to optimum intensity and alignment specifications. It is worth noting here that this process is usually unneccesary if the lasers are run for a minimum of 30 minutes per week.

3.2.2 PIV CCD Camera

For these measurements, double-frame images were acquired with a prescribed delay time (dt) using a Flowmaster 2S type CCD camera[T]. The 12-bit camera provides a 2kx2k pixel resolution and a maximum acquisition rate of 11.8 double-frames/s. The lens mounted to the front of the acquisition camera was a Nikon AF Nikkor 50mm focal length lens[Z]. This provides the ability to adjust the focus and aperture of the light scatter image reaching the CCD. The frame-transfer style CCD employed in this camera allows for two image frames to be captured over a very low time delay.

A light filter[AA] was utilized while acquiring data in order to inhibit ambient light from reaching the camera CCD. This band-pass light filter only allows light within the range emitted by the PIV laser to pass to the CCD, near the 532nm wavelength.

3.2.3 Computer and Programmable Timing Unit

The computer supplied with the LaVision PIV system is a dual Intel Xeon processor machine with an internal Programable Timing Unit (PTU). The PTU onboard the PC was used to control and synchronize the camera's double-frame image acquisition with the pulse of each laser. One image (two frames) per laser pulse cycle (one pulse from each laser head) was acquired. The PTU incorporates all the features of the LaVision PIV software, DaVis. The DaVis software was used to set the image frame-pair time delay (dt), as well as many other settings discussed in Section 3.3.

3.2.4 Aspirator Flow Seeder

The flow seeder[W] used to supply seeding particles to both the primary flow as well as the entrainment flow was a Topas brand Aerosolgenerator ATM 210/H. This aspirator uses high pressure air with a Venturi nozzle to create a very high velocity outside the seeding fluid reservoir and, as a result, draws in the liquid seeder fluid out of the reservoir in a gaseous state. The fluid used here is Bis(2-ethylhexyl) Sebacate (DEHS) which provides a very steady, non-toxic vapor when used with the aspirator. The particle sizes generated, according to the manufacturer specifications, are within the range of $0.2\mu m$ and $0.3\mu m$.

3.3 DaVis PIV Software Calibration and Cross-Correlation Method

The LaVision PIV program, DaVis, was used to acquire all images and ultimately process the image frames into vector fields in these experiments. After the initial alignment of the PIV lasers and camera, there is very little activity which is necessary but not controlled via the computer software, i.e. DaVis. DaVis controls every aspect necessary for proper PIV acquisition and processing including camera calibration, image acquisi-

tion, vector calculation, and vector validation. These processes are outlined and describe in this section. DaVis also offers a multitude of post-processing routines and calculations; however, these post-processing tasks were completed outside of the pre-written LaVision software for these experimental results.

3.3.1 Camera Calibration

Proper calibration of the PIV camera is of utmost importance given that any mis-calibration will be unknown and possibly un-noticeable until much later in the analysis of the results. This process is the only physical link between the real flow field and the ultimate vector field which is calculated. The process begins by constructing a calibration plate[BB] that, when oriented in the desired plane of the data, can be imaged by the PIV camera and used to link the real image plane to that which is recorded by the camera. This calibration grid supplies a known reference distance and location to the acquired calibration image.

3.3.2 PIV Image Plane

The data discussed herein were acquired in two separate image planes. The initial data were acquired at the backstep location (x=0) to analyze the boundary layer and primary inlet flow. The inlet image plane was large enough to span the entire inlet of the primary flow. The second image plane (downstream image plane) was located downstream at 432.5mm<x<734.6mm and spanned from the wall on the high speed side to the low speed side entrainment flow region (-195mm<y<106mm). This downstream image plane provided the data that is of primary interest in these experiments. These image planes are demonstrated in Figure 3.3.

3.3.3 Image Processing Routines - Vector Field Calculation

The images acquired in these experiments were taken using a double-frame double-exposure method. In practice this means that each 'image' acquired is actually two frames which have a set time delay, dt=300µs for these data. A cross-correlation technique is used to map the movement of small clusters of seed particles, within correlation windows, and to assign a distance traveled ($\vec{D}$), see Figure 3.4. This distance and the prescribed time delay combine to form a velocity vector $\vec{V}$:

$$\vec{V} = \left(\frac{\vec{D}}{dt}\right),\tag{3.1}$$

assigned to the interrogated window. Initially, each frame is divided into windows which are cross-correlated with the corresponding window from the other frame. This two-dimensional cross-correlation method provides a correlation map over each window area and the peak correlation level is selected as the most appropriate vector. There are additional methods employed during this process to not only ensure that the most appropriate vector is calculated, but also to ensure that spurious vectors are disallowed or more appropriately calculated as described below.

When processing PIV images it is often useful to have an initial shift of the correlation windows so that the most appropriate vector may be calculated. One method for accomplishing this is to start with a larger window size than is ultimately desired. By first calculating vectors over a larger window, the area is smoothed and a general vector over that area can be used as an initial shift for smaller correlation windows. This larger window is then split into 4 smaller windows and the correlation is calculated again using the initial shift from the larger window, this helps to ensure that the same particle groups are

30

correlated for each iteration. For these data, the initial window size was 128 pixels and the final window size was 16 pixels, each reduction in size is a one-half side-length reduction (128 --> 64 -->32 --> 16 pixels). Another method used to increase the accuracy of the initial shift vector is a re-run of the cross-correlation at each window size using the result of the initial run at that window size. This allows the correlation to take into consideration an initial 'guess' that is of the same window size and increases distance over which the peak correlation search is performed. Also, correlation overlap allows the correlation map to include a percentage of the surrounding area which can aide in proper correlation when particle groups have partially passed into the surrounding windows. For these data the initial correlations were overlapped 25%, and the final correlation windows were overlapped 50%. The final correlation overlap also serves as a method to increase vector resolution (calculated vector density). It allows the correlation windows to be overlapped in order to create more vectors with the same window size. Figure 3.5 demonstrates this increase in vector density with a 50% final interrogation window overlap. In the end, the data acquired here provided cross-correlation vector fields comprised of 65536 vectors (256^2).

There are many vector validation routines which can help to identify and eliminate spurious vectors incorporated into the DaVis software. Two of these routines were employed during these calculations. They are termed the minimum peak ratio and the median filter. The minimum peak ratio validation method ensures that there are no secondary correlation peaks which are near the magnitude of the primary correlation peak. If, for example, there are two local-maximum peaks in the correlation map, and they are of the same order of magnitude, then it is possible that either of the peaks could be the correct correlation. Therefore, the primary correlation peak cannot be validated with confidence.

The ratio of the primary peak to the secondary peak for these validations was required to be greater than 1.2. It is worth noting that the primary and secondary peaks a have the minimum peak subtracted from their levels, this eliminates the influence of any noise that may exist within the image. Therefore, the final calculation of peak ration (Q) is:

$$Q = \frac{P_1 - P_{min}}{P_{2(1)} - P_{min}} > 1.2 \tag{3.2}$$

A second validation method used here, the median filter, examines the results of the correlations surrounding each window and verifies that there is some continuity in the vector field results. For all vectors, the median of the eight surrounding vectors is calculated. Then, from this median, the RMS of the eight surrounding vectors is calculated. Figure 3.6 provides an example vector field that may, depending on the level of acceptable relative RMS, remove and replace the center vector. The median value is used, rather than the mean value, so that the most extreme values do not influence the comparison vector. Also, when the RMS is calculated, the two most outlying points are not included as to not greatly sway the result. For the validations employed here, a vector was removed if the vector was not within the median of its neighbors plus/minus two-times the RMS of its neighbors. Also, the median vector was inserted if the calculated vector was within the median of its neighbors plus/minus 3 times the RMS of its neighbors. These parameters are demonstrated for a non-specific streamwise velocity component vector in equations 3.3 and 3.4.

$$\text{remove: } U_{median} - 2U_{rms} \leq U \leq U_{median} + 2U_{rms} \tag{3.3}$$

$$\text{replace: } U_{median} - 3U_{rms} \leq U \leq U_{median} + 3U_{rms} \tag{3.4}$$

3.4 MATLAB Post-Processing Routines

After calculating and validating complete vector fields from 1000 images, these vector fields were exported from DaVis into MATLAB. Numerous post-processing calculations were completed using MATLAB. From DaVis the coordinates (x, y) as well as the calculated two components of velocity (u, v) were exported, {x, y, u, v}. All other calculations were completed with code written specifically for these experiments by the author.

3.4.1 Ensemble Calculation

Several statistical and numerical calculations were carried out that required information from all 1000 vector fields. One difficulty in calculating the statistical results is the available memory of the processing computer. Due to the large amount of information contained in each vector field (65536x4) and the large number of total data files (1000), each vector field was loaded and summed pointwise. The total value for each vector was then divided by the total number of summed values at each location to find the mean. Once the mean vector field was determined, other field contour variables could be calculated such as the turbulence intensity and vorticity fields.

The vorticity field was calculated from the mean velocity field of all 1000 images. A circulation contour method was used in which a 24-point contour (7x7 discrete grid of points) was used to calculate the circulation. The circulation value was then divided by the area ($\sim$43mm^2 area square block) to arrive at the vorticity at a given central grid point; see Figure 3.7. One caveat of this method arises at the corner points. In essence, each discrete grid point, located at a circulation contour corner, represents a velocity value one-half a grid spacing distance on either side of its location. This means that at the corners, these points only represent one-half a grid spacing in one direction. To account for this, a mean

value was calculated and reorganized halfway between each grid point. In practice, this was accomplished by adding all discrete points around the contour, but only adding half of the value at each corner. The described contour and area calculation is demonstrated, for a non-specific representative 7x7 grid, in Figure 3.7. By using the circulation contour method, each vorticity value was smoothed over a larger area than represented by a single grid-point but the loss in resolution was offset by the gain in data that was included in each calculation. Vorticity calculations were completed using a derivative method as well as circulation integrals with small contour areas, however, these methods proved less effective than the described technique.

3.4.2 Singular Point Mapping and Circulation Calculations

Following thorough ensemble vector field calculation, instantaneous images were investigated to map the location of all singular points. Singular points, as described in section 1.4, are points of discontinuity in a planar flow field. The node and saddle occurrences were mapped from the instantaneous vector field. Also, in a separate investigation, the nodal points traveling at the convection velocity were located from instantaneous images with the convection speed subtracted. By locating these singular points in these two types of instantaneous realizations, statistical representations and characterizations were calculated. The vorticity was also calculated around the nodal points traveling at the convection velocity to represent the size and strength of these large scale, convecting vortical motions.

In order to accurately and efficiently calculate the vorticity around a node at different circulation areas, MATLAB was used for the circulation contour calculations about each node center. The node centers of the data images were manually located and recorded

using streamlines created in Tecplot (discussed in section 3.5), next MATLAB was used to evaluate these points. MATLAB code was written to load these locations, load the appropriate velocity vector field files, and calculate the circulation at increasing square contour areas. The area spacing was increased one grid point in each direction at a time, and the circulation ($\vec{\Gamma}$)and thus the vorticity ($\vec{\omega}$) was calculated based on the contour area (A).

$$\vec{\omega} = \frac{\vec{\Gamma}}{A} \qquad (3.5)$$

The vorticity versus the area, as well as other relationships, were then plotted and evaluated. By using MATLAB, many circulation areas were able to be calculated efficiently and precisely as well as introducing a degree of regularity in the calculations, i.e. square contour areas located at the discrete grid points.

3.5 Tecplot 360 - Contour Plots and Streamlines

Tecplot was used to plot all field contours presented in these discussions, the high quality and customization that this program offers allowed for very professional and appropriate representations of these complicated data sets. One of the most attractive features of the Tecplot software is its streamline integration routine. The software includes the ability to, based on 2 specified variables (u and v here), integrate across discrete grid points and calculate smooth traces that follow the flow path based on the discrete grid points. Figure 3.8 provides a portion of one representative discrete vector field with streamlines which pass between grid points. Discrete data are located only at the orthogonal grid intersections (thick lines), but the streamlines (thin lines with arrows) clearly pass smoothly between many discrete points. This feature was used to manually map all singular points located within the image planes. By mapping these singular points, statistical

investigations of singular point locations, spacings, consistency, and types within each
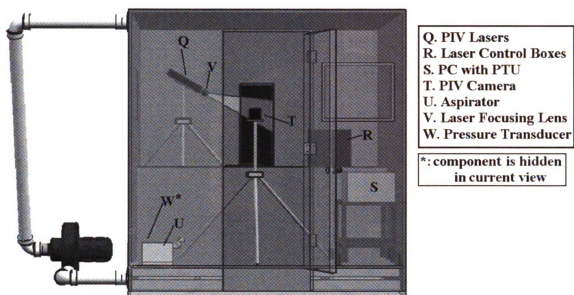
vector field were completed.

| Q. PIV Lasers |
| R. Laser Control Boxes |
| S. PC with PTU |
| T. PIV Camera |
| U. Aspirator |
| V. Laser Focusing Lens |
| W. Pressure Transducer |

| *: component is hidden in current view |

Figure 3.1 PIV house with installed test-section and PIV equipment - Model

Q. PIV Lasers
R. Laser Control Boxes
T. PIV Camera
V. Laser Focusing Lens
X. Laser Divergent Lens
Y. Laser Cooling Lines
Z. Camera Focusing Lens
AA. Light Filter
BB. Installed PIV Calibration Plate
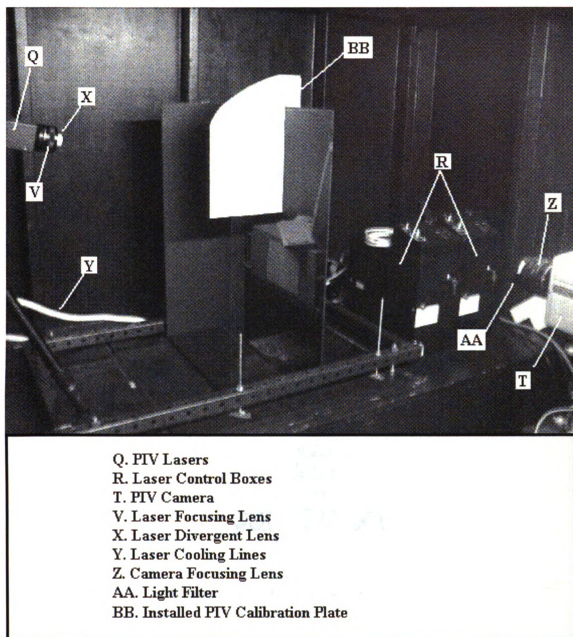
Figure 3.2 PIV house with installed test-section and PIV equipment - Photo
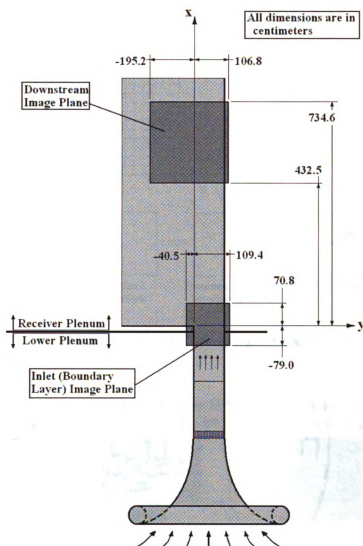
Figure 3.3 PIV Image Plane Locations

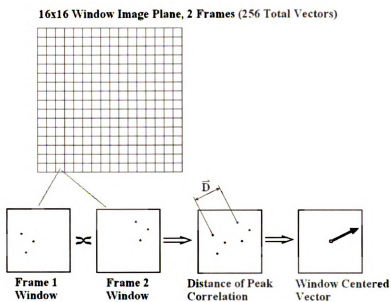**16x16 Window Image Plane, 2 Frames (256 Total Vectors)**

$\vec{D}$

| Frame 1 Window | Frame 2 Window | Distance of Peak Correlation | Window Centered Vector |

Figure 3.4 Cross-Correlation Method

Initial Overlap 0%
Final Overlap 0%

Initial Overlap 50%
Final Overlap 0%

Initial Overlap 0%
Final Overlap 50%

Interrogation Window

Overlap Area

Calculated Vector
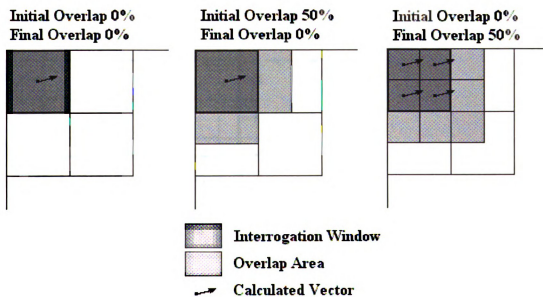
Figure 3.5 Initial and Final Window Overlap Correlations
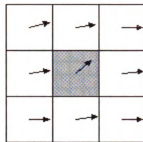
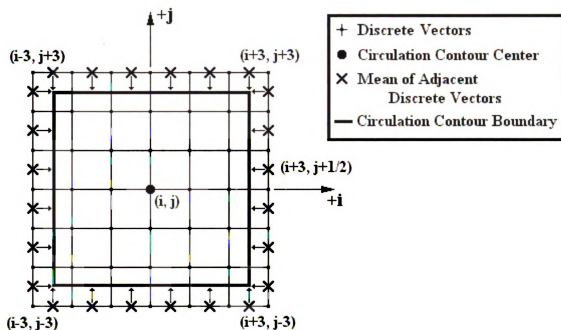Figure 3.6 Median Filter example Vector Field

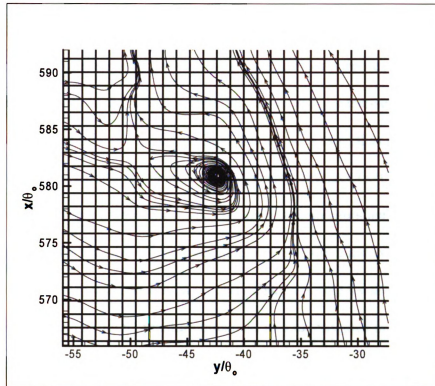Figure 3.7 Circulation Contour of a 7x7 Discrete Grid (6x6 Area)

Figure 3.8 Discrete Grid with Integrated Streamlines

4.0 Boundary Layer PIV Results

An initial investigation into the boundary layer separation region, at the backstep region of the shear layer test-section, was carried out for two purposes. The first was to characterize the quality of the inlet flow entering the shear layer test-section. It was important to verify the inlet flow contained minimal disturbances as well as possessed a mostly uniform streamwise velocity profile across the backstep interface (x=0). A uniform inlet condition is an important criteria for the desired downstream canonical shear layer. The second purpose of the boundary layer investigation was to quantitatively define the initial momentum thickness in order to aide in properly characterizing the downstream shear layer. Specifically, the initial momentum thickness was investigated and found to be $\theta_0=1.11$mm at x=2mm. (This small x>0 value was required to obtain reliable PIV observations.)

4.1 Acquisition and Processing Specifications

As demonstrated in Figure 4.1, the boundary layer PIV image plane was positioned to capture both upstream and downstream of the backstep. Due to obstructions in the PIV camera's view, the usable data range was from -20mm<x<9mm, the blockages can be seen in any representative PIV image such as that presented in Figure 4.2. Due to the positioning of the laser, the data range was ultimately reduced further due to both laser light blockage and reduced laser light intensity, the final data range can be seen in Figure 4.3. All boundary layer PIV results were calculated from the ensemble of 400 vector fields. As discussed earlier, the PIV image discrete grid size was $(256)^2$ points, this provides a resolution of 0.58mm spacing between each discrete grid point. Topologically this image plane has an identical setup to that described in the introduction for the entire sin-

gle-stream shear layer region. This orientation results in three holes in the collapsed sphere on the mid-plane of the test-section. One half-saddle is located at the separation edge of the backstep and, hence, the topological constraint is satisfied as $\chi_{surface}$=2-3= -1.

4.2 Boundary Layer Velocity Contour PIV Results

The boundary layer PIV data results provide a clear indication of the quality of the inlet flow and they adequately define the initial scale for the description of the downstream shear layer. The mean streamwise velocity ($\bar{u}$) calculated over the entire validated data range is presented in Figure 4.4. It is apparent from the representative PIV image in Figure 4.2 that there is high intensity light reflection interference with the results at the backstep (x=0, y=0). This interference appears to be non-existent when moving downstream from x = 0mm to a location of x = 2mm. These data are further investigated in the following section by extracting discrete velocity profiles at multiple downstream locations in close proximity to the backstep.

4.3 Discrete Boundary Layer Profiles from PIV Results

Extracting a streamwise velocity profile across the inlet span from the PIV images allows for further detailed boundary layer profile examination. Figure 4.5 gives the inlet (x=2mm) streamwise velocity profile. Also provided in Figure 4.5 is the streamwise turbulence intensity profile at x=2mm downstream. In examining the inlet profile, there are deviations from a perfectly uniform free stream region profile. However, the detailed measurements will be taken downstream and will focus on the entrainment side of the shear layer, therefore, the slight streamwise inlet velocity profile unevenness will be demonstrated to dissipate upstream of the downstream measurements. Qualitatively, a more uni-

form inlet flow could be achieved, however, this inlet profile will suffice for the intended measurements. The mean streamwise velocity level in the inlet free stream, from point b to point c as denoted in Figure 4.5, is calculated to be $\overline{U}_{o,x=0} = 4.51$ m/s. This is within 2% of the free-stream streamwise velocity ($\overline{U}_o = 4.6$ m/s) at the downstream data region investigated in chapter 5.

Figure 4.6 provides boundary layer profiles at four streamwise locations in the immediate region of the backstep (-10mm<y<25mm). At downstream locations of x = 2mm, 3mm, 4mm, and 5mm the profiles appear to be very similar both qualitatively and quantitatively. Calculating the momentum thickness, defined by,

$$\theta(x) = \int_a^b \left(\frac{u(y)}{\overline{U}_{o,x=0}} \right) \left(1 - \left(\frac{u(y)}{\overline{U}_{o,x=0}} \right) \right) dy \tag{4.1}$$

at both x=2mm and x=3mm downstream arrives at θ_o=1.11mm. For these calculations b was taken to be the location of the local maximum velocity, as seen in Figure 4.6, this occurred at y=10mm. Also, a was taken at y=-0.3mm or slightly to the negative y-side of the backstep location, this is also the location where all four profiles meet and reach a nearly minimum and constant level. This range is supported by Figure 4.7 which represents the associated streamwise turbulence intensities ($\tilde{u}$) levels at the various downstream locations, the spanwise range of -0.3mm<y<10mm roughly defines where the turbulent intensity values arrive at near minimum values of $\tilde{u} = 0.1$ m/s.

The boundary layer results nominally agree well with the Blasius solution with a small negative pressure gradient. Figure 4.8 presents the boundary layer data at x=2mm normalized to Blasius coordinates F' and η.

45

$$F' = \frac{\bar{u}}{\bar{U}_o} \tag{4.2}$$

$$\eta = (0.664)\frac{y}{\theta_o} \tag{4.3}$$

The boundary layer's agreement with the Blasius solution determines that the inlet flow is adequately prepared by the upstream flow conditioning elements.

With the inlet flow sufficiently characterized, it is now possible to investigate the primary region of interest for these data; the downstream entrainment side of the self-similar single-stream shear layer. From the inlet region PIV results, the initial momentum thickness has been determined to be $\theta_o = 1.11$mm, and the inlet profile has been shown to be sufficiently uniform.
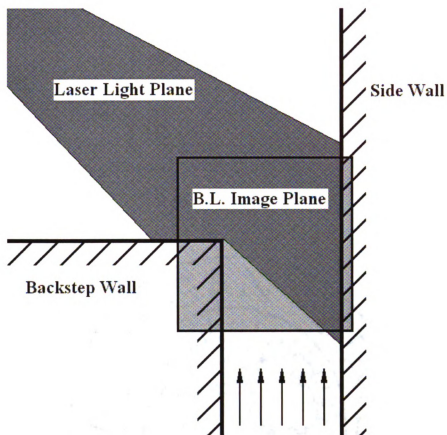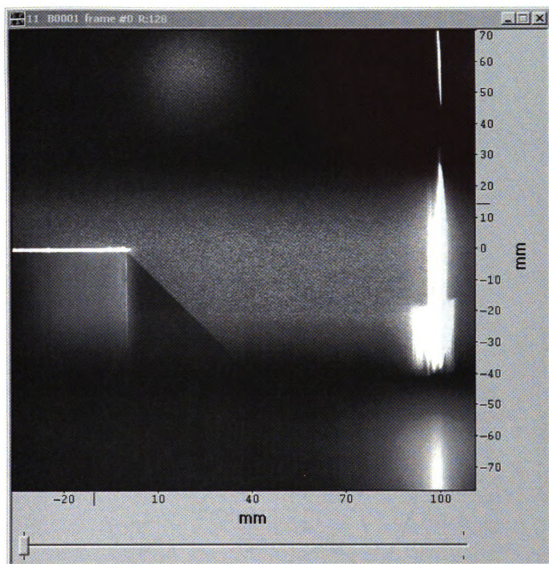
Figure 4.1 Boundary Layer PIV Image Definition

The figure contains the following labels: Laser Light Plane, Side Wall, B.L. Image Plane, Backstep Wall.

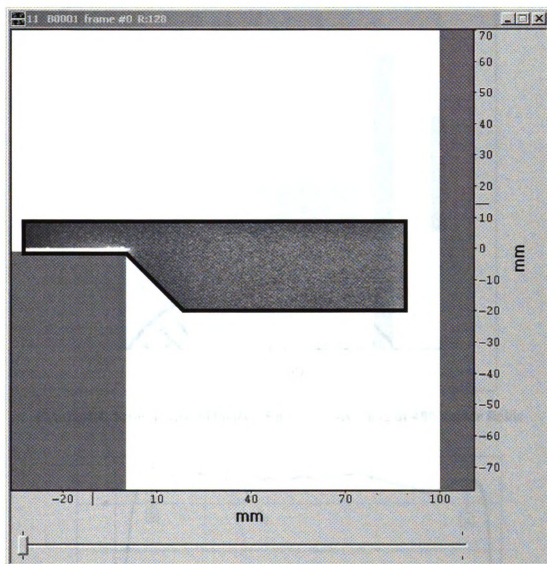**Figure 4.2 Representative Boundary Layer PIV Image**

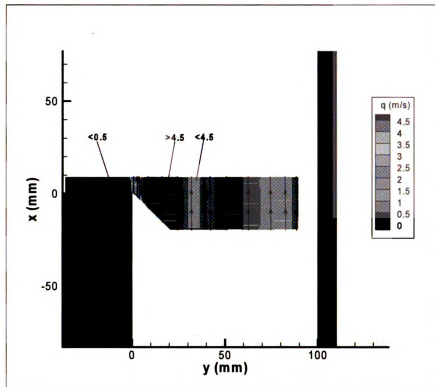**Figure 4.3 Boundary Layer PIV Image - Reliable Image Range**

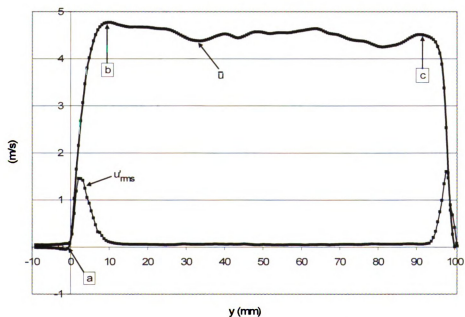**Figure 4.4 Streamwise Velocity - Ensemble Average of 400 vector fields**

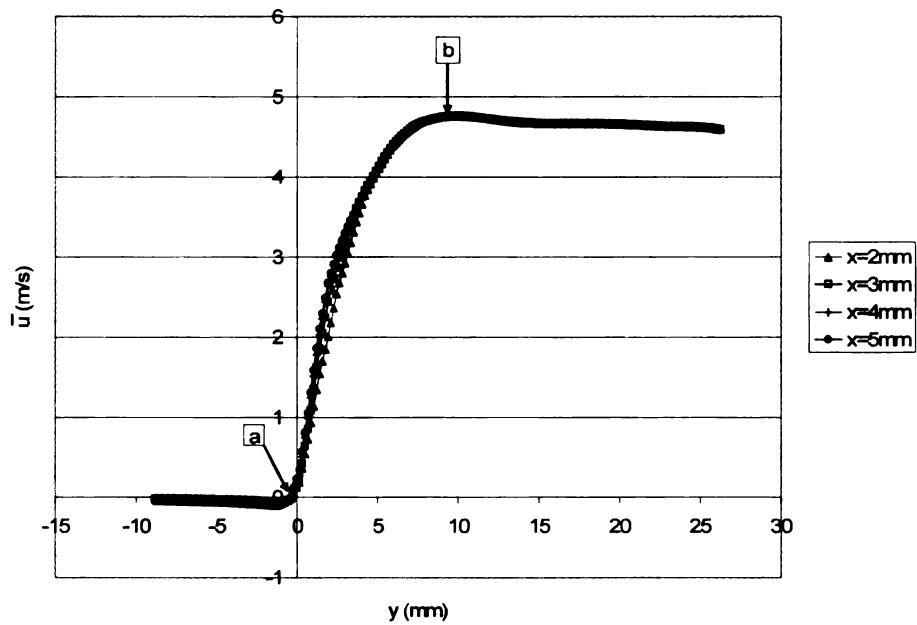**Figure 4.5 Streamwise Velocity and Turbulence Intensity Profiles at the Inlet (x=2mm)**

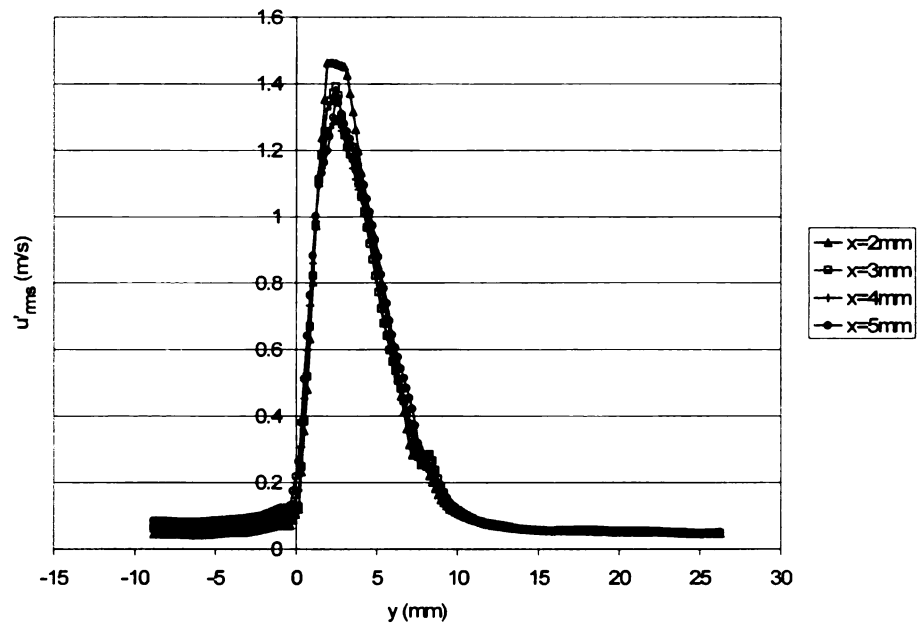**Figure 4.6 Inlet Region Streamwise Velocity Profiles**

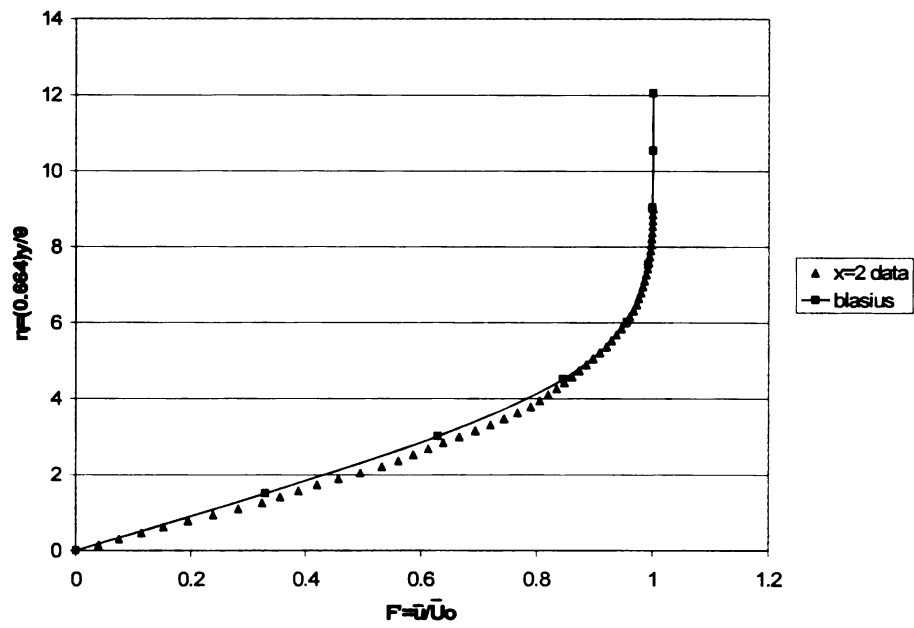**Figure 4.7 Inlet Region Streamwise Velocity RMS Profile**

Figure 4.8 Boundary Layer Data and Blasius Solution

5.0 Downstream Ensemble PIV Results

Detailed investigations of downstream PIV data were conducted to examine the

interaction of the shear layer with the associated entrained fluid. The complete data set

consisted of 1000 dual-frame images, acquired in order to calculate converged statistical

characterizations of the shear layer. These images were processed as described in chapter

2 and all 1000 vector fields, representing 65536 (256^2) discrete vectors per image, were

utilized in the present calculations. The cross-correlation parameters and the employed

settings are presented in Table 1.

Table 1: Utilized Correlation Parameters

Initial Window (pixels)	Initial Window Overlap	Initial Window Iterations	Final Window (pixels)	Final Window Overlap	Final Window Iterations	Correlation Peak Ratio	Median Filter
128^2	50%	2	32^2	50%	3	Q>1.2	2^a & 3^b

a. Velocity vector must be greater than 2 times the RMS of the surrounding vectors in order to be removed (further description in Section 3.3.3)
b. Velocity vector must be less than 3 times the RMS of the surrounding vectors in order to be replaced with the median of the surrounding vectors (further description in Section 3.3.3)

5.1 PIV Vector Field Converged Data Range

5.1.0.1 Downstream Image Plane Definition and Orientation

The image plane utilized for these data is defined by Figure 5.1, which demon-

strates the location and orientation of the downstream image plane and the major sur-

rounding geometry. The positive x-direction is in the primary flow's streamwise direction

and the positive y-direction is oriented such that $\frac{du}{dy}$ >0 in the shear layer, this is demon-

strated in Figure 5.1. Note that, the PIV laser light sheet divergence is not capable of illu-

minating the entire image plane, as is shown in Figure 5.2. The most-divergent lens

(defined in section 3.2.1) was utilized for these measurements, also, the laser head was

maximally displaced in the negative y-direction to allow for the largest area of illuminated particles as possible. The total image area was not reduced due to the existence of reliable data across the entire span of the image. Therefore, the properly illuminated region in the image plane must be identified. A new, smaller measurement domain is defined below.

5.1.0.2 Measurement Domain

Figure 5.2 supplies clear insight into why some of the measurement domain is inadequately illuminated for PIV measurements. Figure 5.3 defines the four regions to be omitted from the inadequately illuminated image in Figure 5.2. Eliminating these regions from the measurement domain assures that the inadequately lit data regions will not influence the nearby regions.

Region #1 defines the upper range of the laser light plane divergence. In the same sense, region #2 defines the lower limit. Region #4 is on the right-hand-side of the image plane, the laser light in this region is directly impinging on the sidewall. In Figure 5.2 it is possible to see not only the highly reflected light near the wall, but the back-corner of the test-section is also affecting the image. The intense light in region #4 prevents proper vector correlations and must be eliminated. Region #3 contains particles that are dimly lit due to the attenuation of the laser light as it passes through the densely seeded primary flow.

The defined region of reliable data is supported by the normalized streamwise turbulence intensity ($\frac{\tilde{u}}{U_o}$) contour plot presented as Figure 5.4. In Figure 5.4, the levels in regions 1-4 give an inaccurately high value. Figure 5.5 provides an example of the final, converged data vector field domain to be investigated. This normalized streamwise velocity vector field and its usefulness will be discussed in further detail in the following sections.

5.2 Ensemble PIV Vector Field Statistics Contours

Using the Tecplot program, contour plots were created by loading the discrete data grid values and using Tecplot's contouring integration routines to smooth across the spaces between the discrete data points. Several statistical and numerical contour fields were calculated including i) the velocity magnitude,

$$q = \sqrt{u^2 + v^2}, \tag{5.1}$$

ii) the streamwise ($\tilde{u}$) and spanwise ($\tilde{v}$) turbulent intensities,

$$\tilde{u} = \left\{ \frac{1}{N-1} \sum_{j=1}^{N} (u - \bar{u})_j^2 \right\}^{1/2} \tag{5.2}$$

where N is the total number of samples (N=1000 for these data) and iii) vorticity,

$$\vec{\omega}_z = \frac{\vec{\Gamma}}{A} = \frac{1}{A} \oint_c (\vec{V} \cdot d\vec{s}) \tag{5.3}$$

Figure 5.5 provides the normalized streamwise velocity ($\bar{u}/\bar{U}_o$) contour. The contour levels represent the normalized streamwise velocities. The streamlines, which are overlaid on the contour plot, are computed from the $\bar{v}$ and $\bar{u}$ components of velocity. Topologically, if seams are placed at the streamline locations as demonstrated in Figure 5.5, then a collapsed sphere with two holes is defined for analysis. The Euler Characteristic of this surface equals zero, therefore, there should be no net singular points contained within the ensemble average of this flow geometry. This is clearly the case in Figure 5.5 where each streamline continuously passes through the image plane. In the following section (section 5.3) the streamwise velocity contour plot will be used to extract discrete streamwise veloc-

ity profiles at various downstream locations in order to investigate the self-similar nature of this shear layer.

The normalized mean vorticity field, given in Figure 5.6, represents a well converged shear layer region. Equation 5.4 demonstrates the method by which the vorticity was normalized.

$$\text{Normalized Vorticity} = \frac{\overline{\omega}_z \overline{\theta}(518\theta_o)}{\overline{U}_o} \qquad (5.4)$$

The mean free-stream velocity ($\overline{U}_o$ = 4.6 m/s) and the momentum thickness $518\theta_o$ downstream ($\overline{\theta}(518\theta_o)$ = 0.0196 m) were used as characteristic values for the vorticity normalization. These vorticity levels are calculated using a 7x7 discrete point contour around a center discrete grid point as described in section 3.4.1.

As a point of interest, it is noted that the angle from which the low speed side entrainment fluid approaches the shear layer has a much larger streamwise velocity component outside the shear layer than was expected. It was expected that the entrained fluid would approach from a much more spanwise direction and undergo a more aggressive turn as it came in close proximity to the edge of the shear layer.

5.3 Discrete Velocity Profiles and Isotach Levels

Discrete data, distinctions: $\overline{u}(y)$ and $\tilde{u}(y)$, were extracted from the smooth contours described in section 5.2. These distributions allow the quality of the single-stream shear layer to be assessed.

5.3.1 Discrete velocity profiles at various downstream locations

56

Velocity profiles were extracted from the smoothed streamwise velocity contours at streamwise locations of $x=495\theta_o$, $513\theta_o$, $531\theta_o$, $549\theta_o$, and $567\theta_o$. These profiles stretch from $y=-169\theta_o$ to $y=85\theta_o$ in the spanwise direction. There were 200 discrete, evenly spaced points extracted for each profile and therefore the point-to-point spacing was $1.28\theta_o$. These dimensional profiles can be seen in Figure 5.7 along with the associated turbulence intensities at the same locations, note the separate ordinates for the mean (LHS) and rms (RHS) levels. It is worth noting that the maximum streamwise velocity level is $\overline{U}_o = 4.6$ m/s. It was expected that the streamwise velocity in the far field entrainment fluid would be very near zero; the data do not appear to fully satisfy this expectation and this will be discussed in further detail later. It will suffice for now to say that the domain bounded by the isotachs: $\overline{u}=(0.13)\overline{U}_o=0.6$ m/s to the free stream ($\overline{u}=\overline{U}_o$), the shear layer can be thought of as single-stream in nature.

The momentum thickness at various streamwise locations, $\theta(x)$, is calculated from each of these profiles. The momentum thickness versus downstream location is plotted for five downstream locations in Figure 5.8. Focusing on the momentum thickness calculated from $\overline{U}_o$ to 13% of $\overline{U}_o$, the growth rate is $d\theta/dx=0.032$. This growth rate is indicative of a single-stream shear layer. Morris (2003) reported that for a self similar single-stream shear layer, the growth rate $d\theta/dx$, was found to be 0.035, and Hussain & Zaman (1985) found a value of 0.032. The present results agree with the latter value. As was pointed out earlier, the streamwise component of velocity in the entrainment region does not appear to approach a constant, nearly zero, level. When the momentum thickness is calculated across the entire spanwise data range, $d\theta/dx$ decreases to 0.019. These observations and calculations lead to the assertion that, to the high speed side of the $(0.13)\overline{U}_o$ isotach, the

57

flow is a single-stream shear layer in character. Figure 5.9 demonstrates the growth rate for isotach levels very near the $(0.13)\overline{U}_o$ isotach. The growth rate (slope) of increases from the higher isotachs to a level of 0.032, which is appropriate as more of the shear layer region is included in the momentum thickness integration. However, to the growth rate (slope) for the isotach levels lower than $(0.13)\overline{U}_o$ begin to decrease which is inappropriate for a single stream shear layer. Therefore Figure 5.9 supports the assessment that flow system is single-stream shear layer in nature from $\overline{u}/\overline{U}_o = 0.13$ to 1.0. .

5.3.2 Single-Steam versus Two-Stream Shear Layer System

After initial analysis of the data acquired from the experimental setup, it becomes clear that the flow system is not a simple, single-stream shear layer. Figure 5.10 provides the, now modified, assessment of the flow system that has been developed. Due to the spatial constraints within the PIV facility, it appears that the primary flow has caused a secondary driven flow which recirculates within the receiver plenum of the PIV facility. The existence of this recirculation was confirmed with a smoke trace placed at the locations shown in Figure 5.10. As demonstrated by the growth rate calculations, the region to the $+y$ side of the $(0.13)\overline{U}_o$ isotach can be analyzed as a single-stream shear layer, and any analysis completed outside this range must be done with this secondary flow structure taken into consideration. The mean velocity magnitude contour is presented in Figure 5.11 with the distinction of the range which is to the high speed side of the $(0.13)\overline{U}_o$ isotach.

5.3.3 Normalized Discrete Profiles

By normalizing the streamwise profiles by $\overline{U}_o$ at each streamwise location and transforming the y-coordinate to η, defined by:

$$\eta = \frac{y - y_{1/2}}{\theta_{13}(x)}, \tag{5.5}$$

the streamwise velocity profiles collapsed to a single profile. $\theta_{13}(x)$ is defined as the streamwise location's momentum thickness from the free stream to 13% of the free stream. The variable, $y_{1/2}$, is defined to be the y-location where one-half of the free stream velocity ($\overline{U}_o/2$) occurs. Figure 5.12 presents the normalized velocity profiles as well as the normalized turbulence intensities, both quantities are normalized by the maximum mean streamwise velocity ($\overline{U}_o = 4.6$m/s). These normalized profiles collapse and agree very well both qualitatively and quantitatively with published results such as those in Spencer (1970 Ph.D. Thesis) and Jones et.al. (report). Specifically, the maximum normalized turbulence intensity in the present data is $\tilde{u}/\overline{U}_o = 0.18$ which is in agreement, albeit on the high end, with published results such as Jones ($\tilde{u}/\overline{U}_o = 0.19$), Wignanski and Fiedler (1970) ($\tilde{u}/\overline{U}_o = 0.176$), and Liepman and Laufer (1947) ($\tilde{u}/\overline{U}_o = 0.15$). From these results, the shear layer inside of $(0.13)\overline{U}_o$ and between streamwise distances of x=495θ_o to x=567θ_o demonstrates the features of a self-similar single-stream shear layer.

5.3.4 Isotach Definition Results

Isotach levels were created using discrete points from the smooth streamwise velocity contour in order to further characterize the present flow in relation to a SSSL and the outer region. In order to create the isotach levels, discrete points were extracted at 9.01θ_o intervals starting at x=486θ_o and continuing to x=567θ_o, these ten points were taken at the location of an isotach at each streamwise location. From these ten points a linear fit was then applied and the linear trendline was extrapolated to x=0. These data show that all isotachs from $(0.13)\overline{U}_o$ to $(0.95)\overline{U}_o$ converge to a "point" very near the separation

lip. It should be noted that some discrete points seemed unindicative of the general 10-point trend and these points were discarded, however, a minimum of 7 points were employed for all isotachs. Figure 5.13 presents these isotachs for 10, 11, 12, 13, 14, 15, 20, 30, 40, 50, 55, 60, 65, 90, and 95 percent of $\overline{U}_0$. These data clearly, combined with the growth rate assessment, support the single-stream shear layer's existence within the described range: $(0.13)\overline{U}_0 \rightarrow \overline{U}_0$.

Isotach levels were developed to provide a method by which to interpolate between determined isotachs and collapse singular point locations in the downstream region. By developing this downstream point isotach fit, the singular point locations are allowed to be based solely the associated spanwise location. An exponential fit was developed based on the slope from a downstream point location to the origin (x=0,y=0). These slopes were then used to develop an interpolated fit. Figure 5.14 presents this fit overlaid on the discrete isotach vs. slope points. The developed fit involves the sum of two exponential functions in the form demonstrated below:

$$isotach = a \times e^{(b-slope)} + c \times e^{(d-slope)} \tag{5.6}$$

Equation 5.6 is utilized in conjunction with the fit constants located in Table 2 to reduce the singular points in chapter 6 to a normalized streamwise location.

Table 2: Slope to Isotach Fit Constants

Constant	Value
a	-57.72
b	0.00118
c	81.01
d	-0.07305
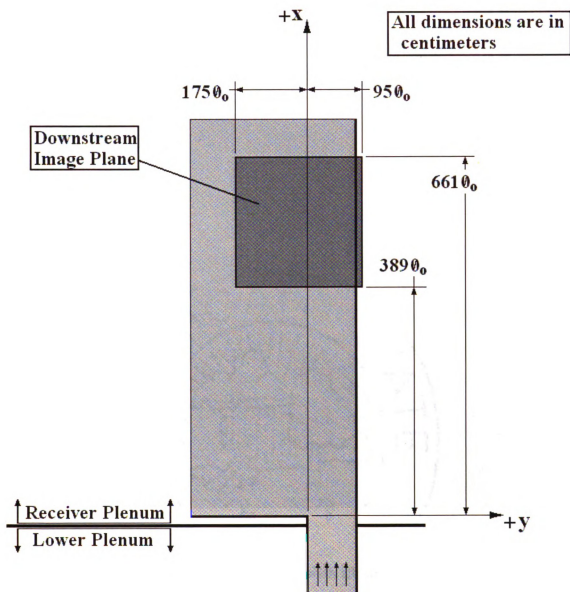
Figure 5.1 Downstream Image Plane
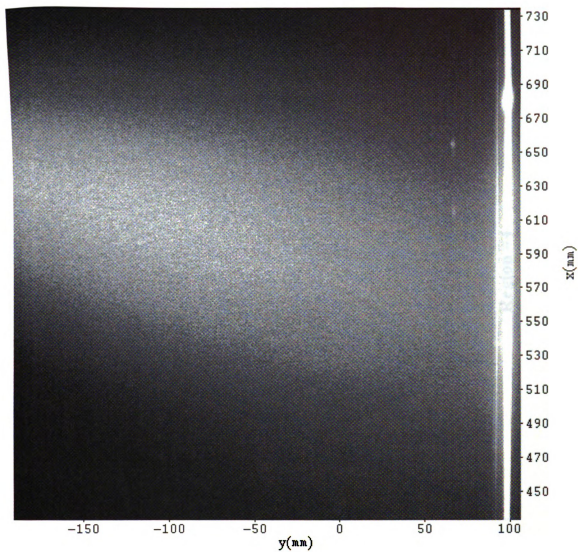
Figure 5.2 PIV Image Frame with Illuminated Particles
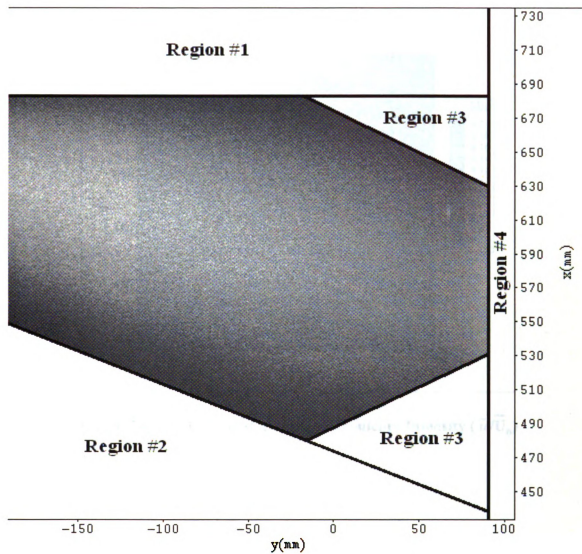
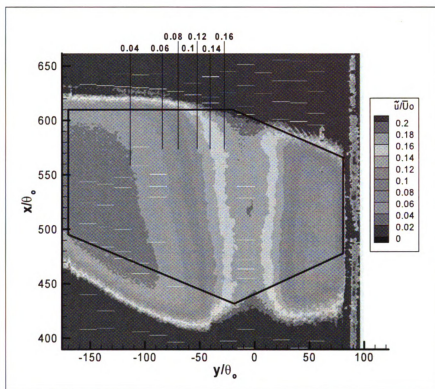**Figure 5.3 PIV Image Plane with Eliminated Data Regions**

63

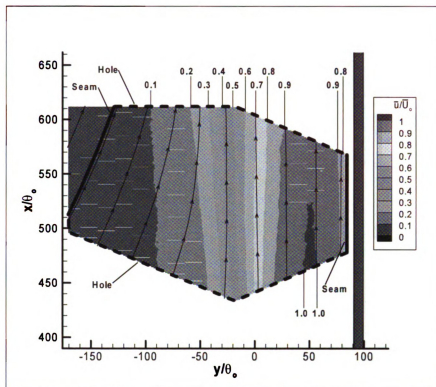**Figure 5.4 Normalized Streamwise Turbulence Intensity ($\tilde{u}/\overline{U}_o$)**

Figure 5.5 Normalized Streamwise Velocity Contour ($\overline{u}/\overline{U}_o$)
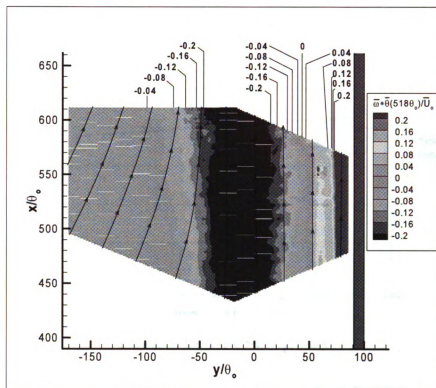
Figure 5.6 Normalized Vorticity Contour $(\overline{\omega}*\overline{\theta}(518\theta_o)/\overline{U}_o)$
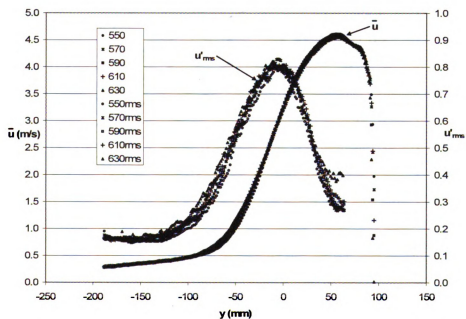
Figure 5.7 Dimensional Velocity and Turbulence Intensity Profiles
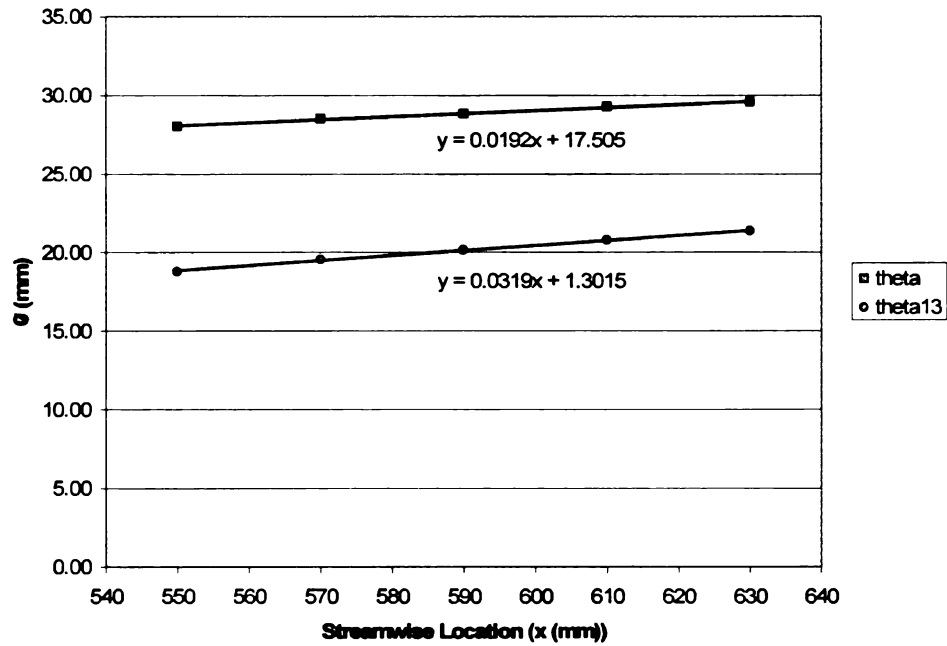
Figure 5.8 θ vs. x and θ_{13} vs. x
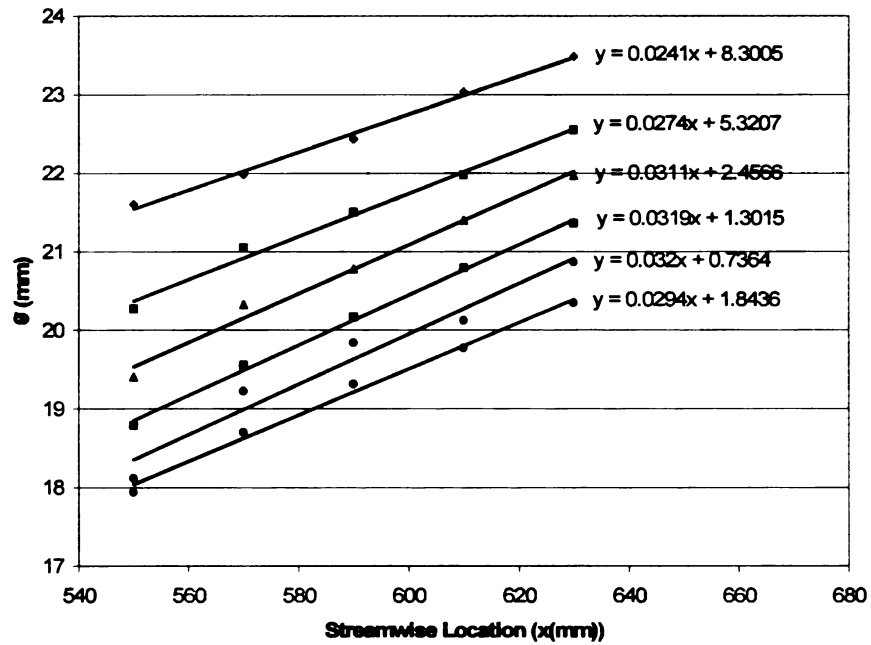
Figure 5.9 Growth Rates at Various Isotach Levels
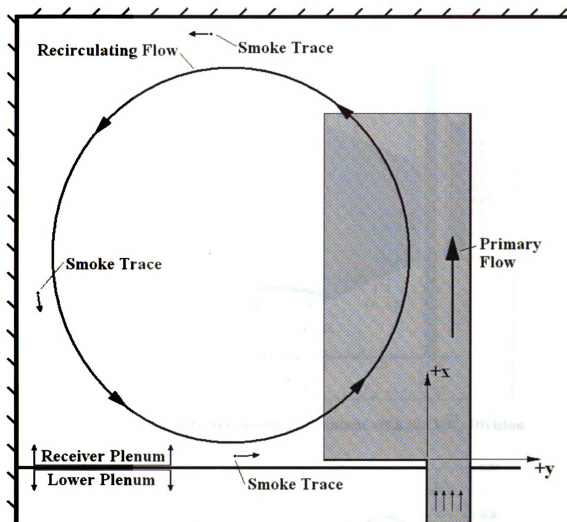
Figure 5.10 Modified Flow System with Smoke Trace Indications

68
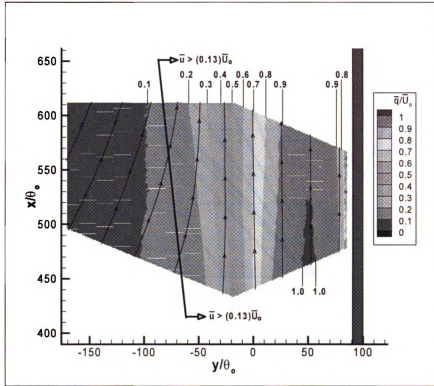
Figure 5.11 Velocity Magnitude ($\bar{q}$) Contour with $(0.13)\bar{U}_o$ Division
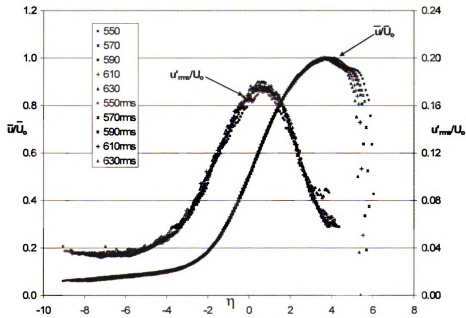
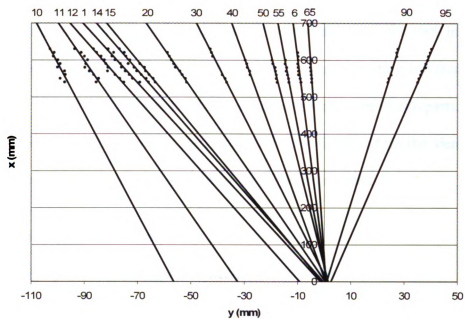**Figure 5.12 Normalized Velocity and Turbulence Intensity Profiles**

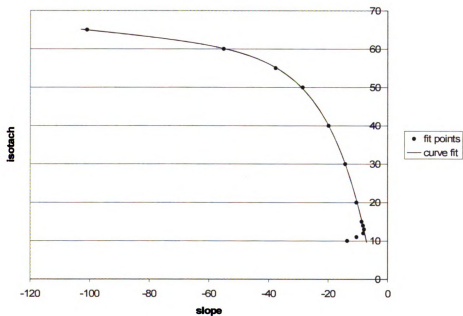**Figure 5.13 Isotach Levels**

Figure 5.14 Isotach vs. Slope Curve Fit

6.0 Singular Point Identification

The identification of singular point locations was carried out for 1000 instantaneous PIV vector fields. This identification involved manually locating and recording the centers of all isolated singular points. The investigations were done in two parts: (i) identification of nodes and saddles within instantaneous vector fields and (ii) the identification of large-scale nodes traveling downstream at the convection speed.

6.1 Node-Saddle Identification

6.1.1 Topological Discussion of Instantaneous Vector Fields

The identification of nodes and saddles is demonstrated in Figure 6.1 which provides a representative instantaneous PIV vector field. Figure 6.1 also demonstrates streamlines based on the vector field and the associated topological considerations. As can be seen in the collapsed sphere assessment of Figure 6.1, there is a clear inlet-hole and an outlet-hole and the seams here are represented by streamlines that clearly bound the isolated domain. In Figure 6.1, the streamlines provide insight into the flow path, all streamlines clearly enter and/or exit their respective holes. The addition of two holes and no handles to the collapsed sphere yields an Euler Characteristic of zero, $\chi_{surface} = 0$. That is, there can be no *net* nodes or saddles, or more explicitly, nodes and saddles must exist in pairs. Therefore, for proper singular point accounting, every node must have an associated saddle or vice-versa. This topological accounting cannot be properly carried out if the flow does not both enter and exit uniformly to the inlet and outlet holes. Figure 6.2 offers an instantaneous vector field which does not provide a uniform inlet hole. It is possible to analyze the highlighted region and utilize many holes and seams, which will result in many nodes and half-saddles. For the present analyses, images which did not properly sat-

71

isfy this simple, uniform inlet and exit condition were discarded. There were a total of 151 of the original 1000 images that were not investigated further due to their complexity near the border of the data range.

In addition to the identification of all singular points contained within a properly collapsed sphere, all nodal singular points were characterized by their type as defined by Perry & Chong (1987). In this reference nodal points are described to have five possible definitions, Figure 6.3 demonstrates these five types of nodes as they apply to two-dimensional fluid flow. These descriptions of node types are taken from Perry & Chong (1987). Figure 6.4 provides a blown-up view of the singular points contained within Figure 6.1. A collapsed sphere is developed again in Figure 6.4 and by the same assertions as outlined for Figure 6.1, all singular points must exist in pairs. There are a total of five nodes located in Figure 6.4 and each has an associated saddle. The nodal points are labeled according to their node-type in Figure 6.4, labeling appears on the right-hand-side of the figure, outside of the data range. The saddle points in Figure 6.4 are also labeled, these are labeled "S" on the top of the image. As expected, there are 5 saddles within the collapsed sphere.

6.1.2 Locations of Nodes and Saddles

After manually locating and logging the location of all singular points, their locations were plotted as seen in Figure 6.5. Nodes are represented by circles and saddles are represented by crosses. It is clear from Figure 6.5 that singular points exist at all streamwise locations. Figure 6.5 also provides isotachs, as defined and discussed in chapter 5, as a relative reference. A distinct feature of these results is the complete lack of any singular points in the positive-y-region through all 1000 images.

Figure 6.6 represents the location of the saddle points relative to their associated node. The associated node was located at the plot origin. This node-to-saddle spacing will be investigated further in section 6.1.3 where all singular points have been collapsed to a single relative streamwise level. It is worth noting here that the node/saddle combination is one selected during the singular point identification, there is no 'right' answer for which node should combine with any specific saddle. In general, as a convention, the nearest saddle was chosen to combine with a node unless there was a clear flow-field reason to choose a different pairing combination. An example of this, see Figure 6.7, involved a very large node with a nearby saddle which was very close to the node center. However, a different saddle is clearly "more-involved" in the node's flow structure. Specifically, node #1 is clearly closer to both saddles #2 and #3 than to saddle#1. However, node #1 is clearly the major contributor to the large flow structure and therefore saddle #1 was chosen as it's pair. Nominally 5% of the assessed pairs required such judgements to be made.

6.1.3 Collapsed Singular Point Statistics

Statistical characterizations of the singular point locations were made using the slope-to-isotach fit developed and described in section 5.3.4. This fit was used to interpolate between manually determined isotach levels and eliminate the dependence of the data upon its streamwise dimension. In reducing the singular points to a single streamwise level, the location is based purely upon the singular points' spanwise location or, more appropriately, the associated isotach for a given streamwise and spanwise location. Figure 6.8 presents the normalized distribution of nodes versus the assigned isotach. The nodes in this distribution were limited to those that were within the single-stream shear layer region[1] and below the $x=585\theta_o$ streamwise level. After this subset of nodes was deter-

mined, the total number of usable nodes was 1154, as opposed to the 2560 total nodes that were identified.

Figure 6.9 provides the normalized distribution of node-to-saddle distance. The abscissa in this figure is presented on a logarithmic scale. Once again, the 1154 single-stream shear layer node subset was used. The mean of this distribution was calculated to be $d_{N/S}/\theta(x) = 0.1884$.

6.2 Identification of Nodes at the Convection Speed

In order to properly identify the location of nodes moving downstream at the convection velocity, the convection velocity was subtracted from the streamwise velocity contours. This convection velocity was calculated from the $0.13\overline{U}_o$ level to $\overline{U}_o$:

$$\overline{U}_c = \frac{\overline{U}_{13} + \overline{U}_0}{2} = \frac{0.6 + 4.6}{2} = 2.6\frac{m}{s} \tag{6.1}$$

The streamlines, which were created using the relative streamwise velocity, quite clearly revealed the large scale nodes in the convecting reference frame. Figure 6.10 provides a representative instantaneous vector field in the convecting reference frame. These new contours were investigated to map the large scale convecting nodes such as that seen in figure 6.10. Figure 6.11 provides the topological considerations for these convection velocity contours. In these flow fields there are 4 total holes, 2 inlet holes and 2 outlet holes. Since the vector field at a topological hole must be unidirectional, there are seams located along streamlines at the top, bottom, and sides of the contour. The Euler Characteristic is -2 for the indicated surface. The half-saddles at the central region streams have

---

1. As described in section 5.3, this region is bounded by the isotachs: u/U_o=0.13 and 1.0.

been described by Foss (2007). Alternatively, it would be possible to simply identify a collapsed sphere surrounding the node for an Euler Characteristic of 2.

6.2.1 Vorticity Calculations for Individual Convecting Nodes

There were 917 total large-scale, convecting nodes located in the 1000 vector fields investigated in the absolute reference frame. The focus of these identification data will be on the large scale nodes, therefore, no saddle locations are documented. Contour circulation calculations were completed by mapping the node centers. Using MATLAB code written for these investigations, the vorticity as the circulation contour area was increased was quantified, see equation 6.2 for this relationship.

$$\bar{\omega}_z = \Gamma / A \qquad\qquad (6.2)$$

The method by which these mean vorticity calculations were completed over various areas is outlined in chapter 3. This method involved calculating the circulation about a 7x7 discrete grid of data points which arrives at a mean vorticity value over the circulation contour area. Figure 6.12 presents the mean vorticity level as the area increases, Figure 6.12 also provides the total number of samples that were incorporated into the mean at each area. This total level changes due to the fact that the node centers are often not in the center of the image plane, therefore circulation calculations could only be completed until one corner of the square circulation contours reached the edge of the data range. The circulation level was no longer calculated once an edge of the data domain was encountered. Figure 6.13 demonstrates a non-centered node with the associated largest circulation contour area that could be calculated. Consider, if this node had been centered within the data domain, many larger circulation areas could have been calculated and included in the mean vorticity for those areas. It is expected that the vorticity values would reach a con-

75

stant level as the area increases, this appears to occur where the area reaches 1×10^4 mm^2. This area would correspond to a contour side length of 100 mm. As can be seen in the representative velocity profiles in Figure 5.7, this is very nearly the width of the shear layer in measurement domain.

When analyzing individual image contours, the vorticity level, as the circulation contour area is increased, seems to nearly always reach a constant level when large enough contour areas are available. However, this minimum vorticity level and the area at which it is finally realized varies for each node. This would seem to account for the slow decrease in the mean vorticity level in Figure 6.12. Figure 6.14 provides traces for a group of ten vorticity vs. contour area investigations and clearly supports the assertion that individual vorticity levels seem to reach a stable level as the area increases. However, in some cases, the computational domain reaches the edge of the data domain prior to reaching the stable level. In these traces, the vorticity value was immediately set to zero once a data domain edge was encountered. Note that these zero levels were not included in the calculated mean vorticity. Figure 6.14 demonstrates two highlighted cases, A and B. Case A involved sufficient contour area evaluations to reach a nearly constant minimum vorticity. In contrast, case B encounters a data domain edge prior to reaching a constant vorticity.

In analyzing these mean vorticity vs. contour area results, the minimum vorticity level as well as at what contour area this level occurs provide insight into the character of the convecting nodes. Figure 6.15 provides the distribution of the minimum vorticity level reached for the investigated set of nodes. This demonstrates the large range of values for the minimum (maximum magnitude) vorticity level. The normalized mean minimum vor-

ticity is $\left\langle \dfrac{\overline{\omega}_z \theta (x = 518 \theta_o)}{\overline{U}_o} \right\rangle = -17.6$. Also, Figure 6.16 demonstrates the area at which the

minimum vorticity level is reached. In these cumulative levels, a large portion of the minima (~30%), occur at very small areas. This high number of instances at the lower areas is most likely a relic of the node centers encountering a domain edge, this will result in a minimum level which is still increasing but cannot be calculated further. Therefore, an investigation which first determines if -- a large enough circulation contour area was utilized to reach a constant vorticity level -- was carried out.

In order to determine if a constant vorticity level was attained for a given node circulation contour area range, a third-order polynomial fit was applied for each circulation vs. area (L^2) investigation. The derivative with respect to the circulation contour area of this fit was taken to arrive at a second-order 'circulation-derivative' polynomial function. The relation of circulation contour area, circulation value, and mean vorticity is provided in equation 6.2.

$$\Gamma = \langle \omega_z \rangle (L^2) \qquad (6.3)$$

The derivative of this relation with respect to circulation contour area is given in equation 6.3.

$$\frac{d\Gamma}{d(L^2)} = \langle \omega_z \rangle \qquad (6.4)$$

It is clear from Equation 6.3 that this circulation derivative is representative of the mean vorticity for a given circulation area. Figure 6.17 provides five representative circulation-derivative vs. area conditions. Employing Equation 6.3 it is apparent that, where these quadratic polynomial traces reach a minimum level, the mean vorticity has reached a constant level. For these results, there were a total of 917 nodes identified. Of these nodes, 394 circulation contours reached a constant vorticity level according to this method. Fig-

ure 6.18 provides the distribution of normalized circulation contour size at which the constant mean vorticity was reached. The mean size, normalized by the momentum thickness at the streamwise location of the node center, is $\langle \frac{L}{\theta(x)} \rangle = 3.34$. Figure 6.19 provides the normalized mean vorticity strength, at the level where the circulation-derivative reached a constant level. The mean of this distribution is $\langle \frac{\bar{\omega}_z \theta(x = 518\theta_o)}{\bar{U}_o} \rangle = -20.37$. As a relative measure, Figure 6.20 provides the normalized distance of the location of the node centers relative to the $(0.5)\bar{U}_o$ isotach. The mean of this normalized distance is

$\langle \frac{y_c}{\theta(x)} \rangle = 0.26$.
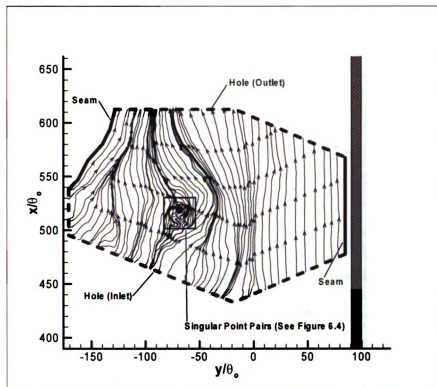
Figure 6.1 Representative Instantaneous Vector Field - Topologically Valid
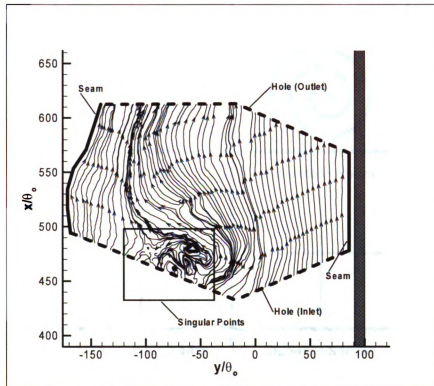
Figure 6.2 Representative Instantaneous Vector Field with "Edge Problems"
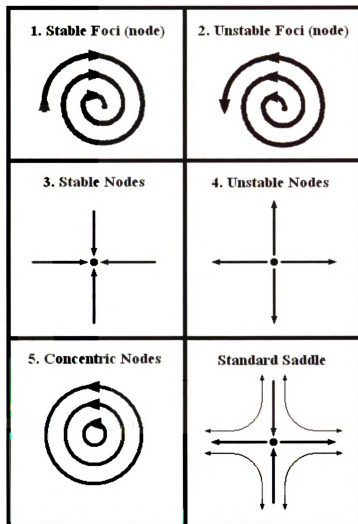
Figure 6.3 Types of Singular Points (Descriptions from Perry & Chong (1986))
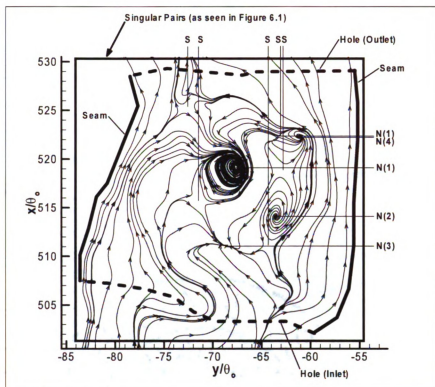
Figure 6.4 Node (rhs) Type Examples with Saddles (top)
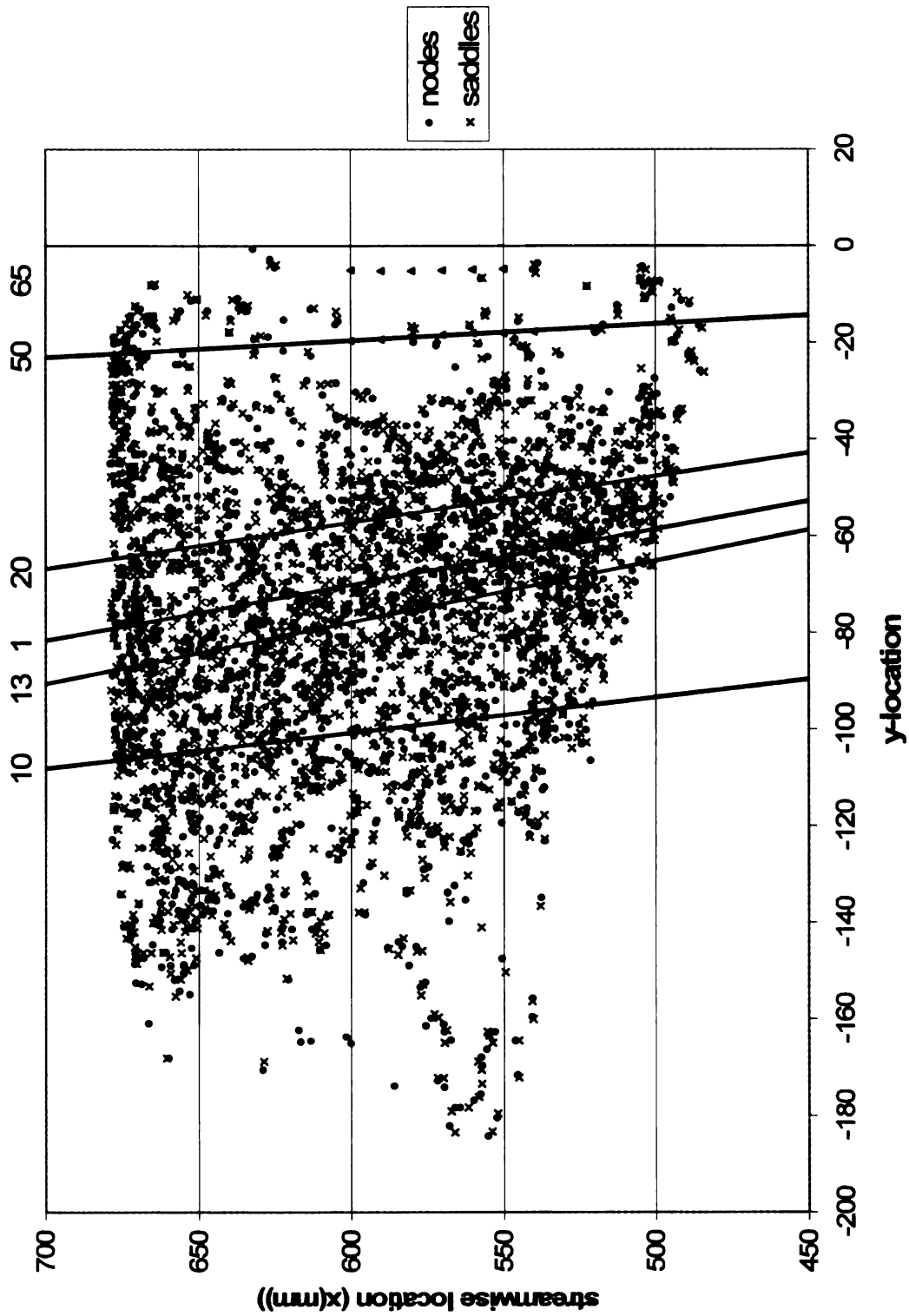
Figure 6.5 Node and Saddle Identification with Selected Isotachs
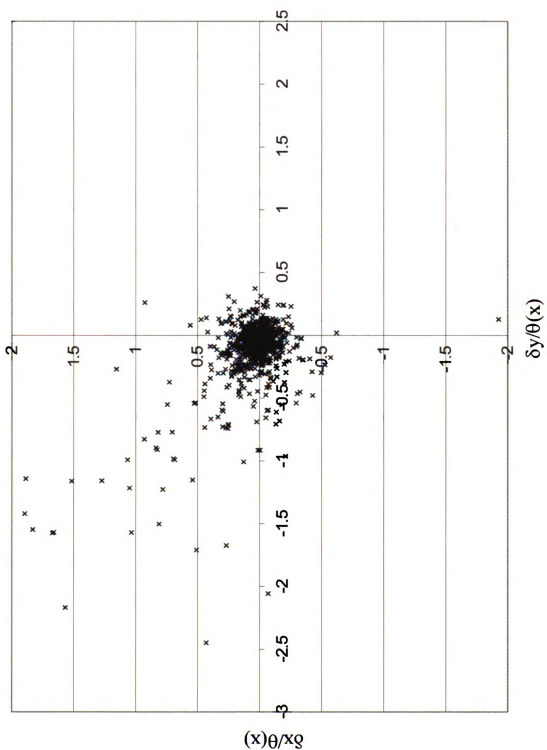
Figure 6.6 Saddle Location Relative to its Associated Node

$$\langle \frac{\delta y}{\theta(x)} \rangle = -0.0933 \qquad \langle \frac{\delta x}{\theta(x)} \rangle = 0.0415$$
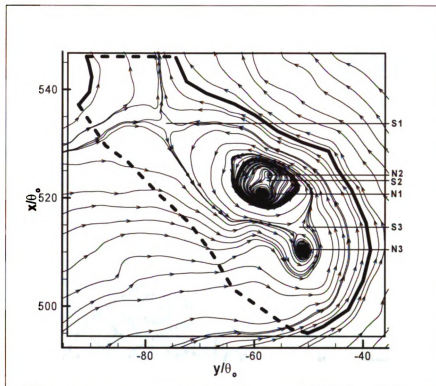
Figure 6.7 Node-Saddle Pairing Example
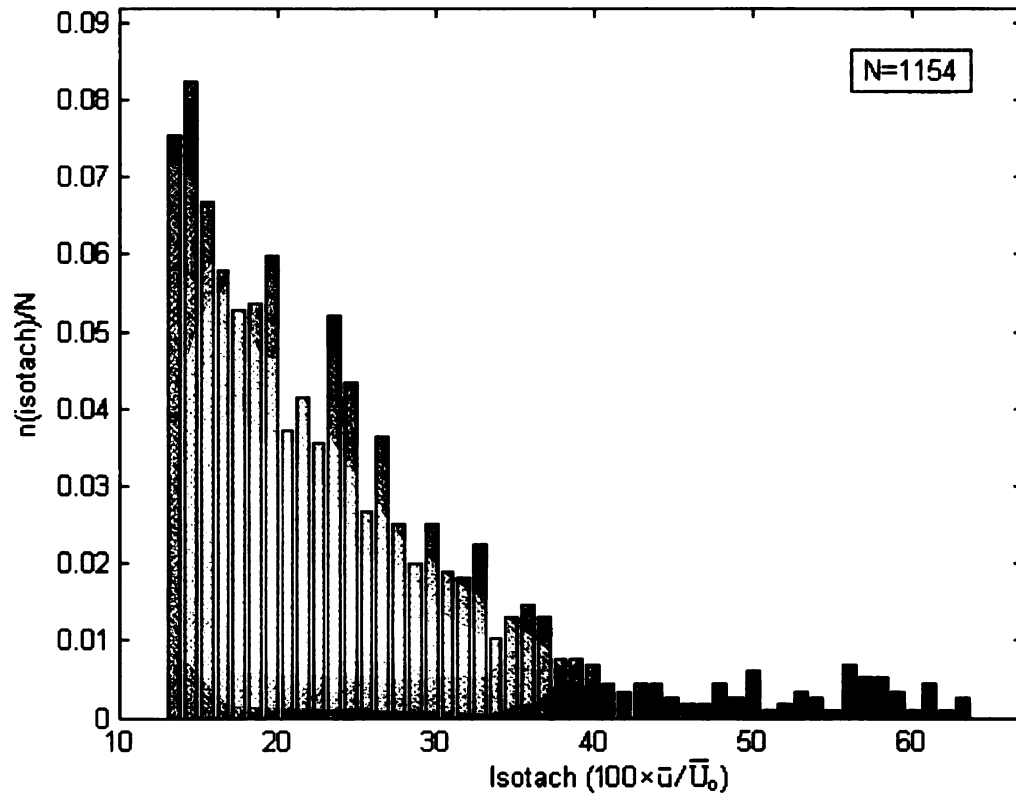
Figure 6.8 Distribution of Nodes in a given Isotach Range - For the $0.13<\overline{u}/\overline{U}_0<1.0$ "single stream shear layer" domain
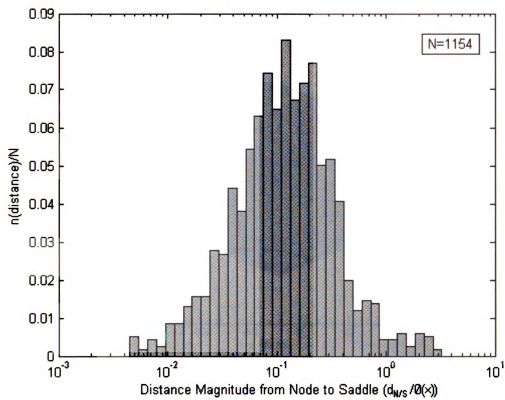
Figure 6.9   Distribution of Node-to-Saddle Distance
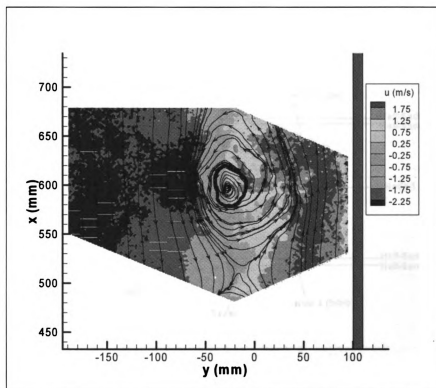
Figure 6.10 Streamwise Velocity Contour - Convection Velocity Reference Frame
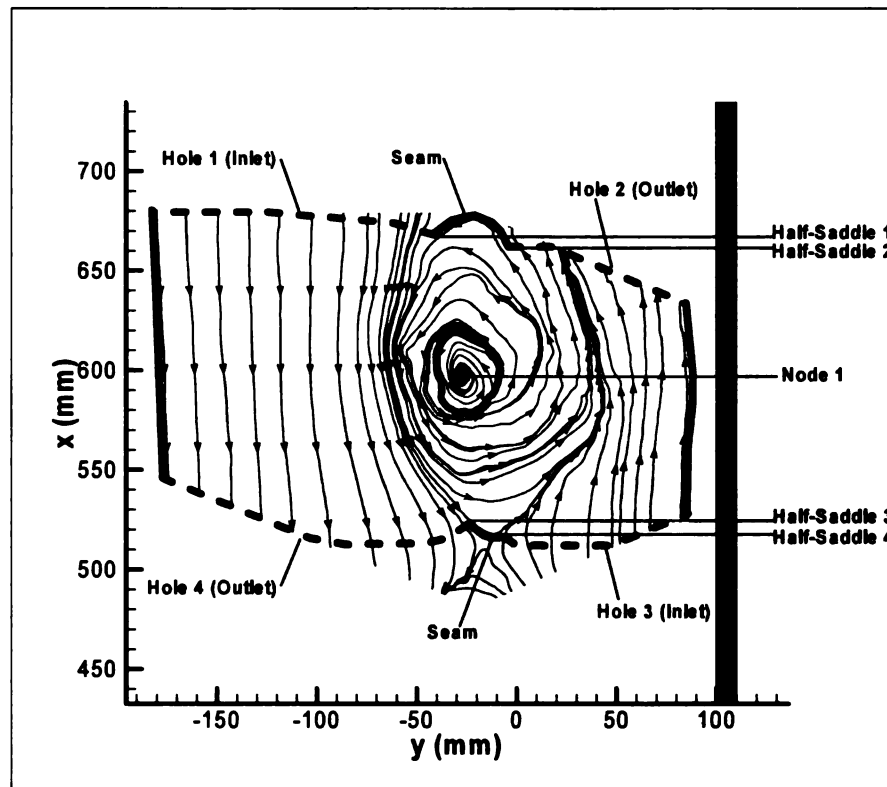
**Figure 6.11 Streamwise Velocity with Topological Considerations - Convection
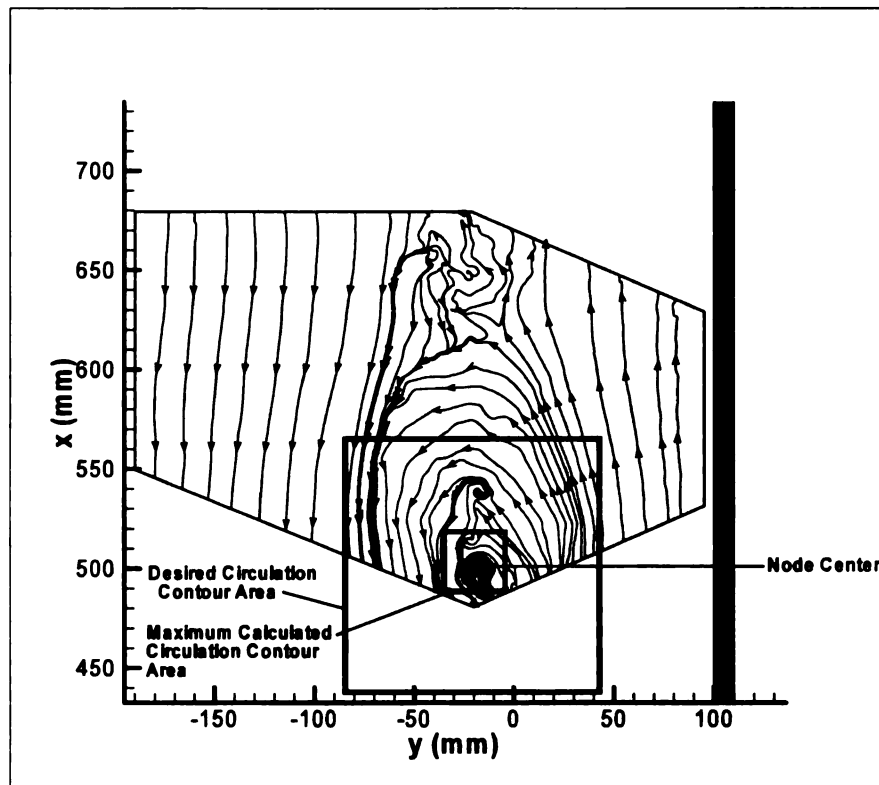Velocity Reference Frame**
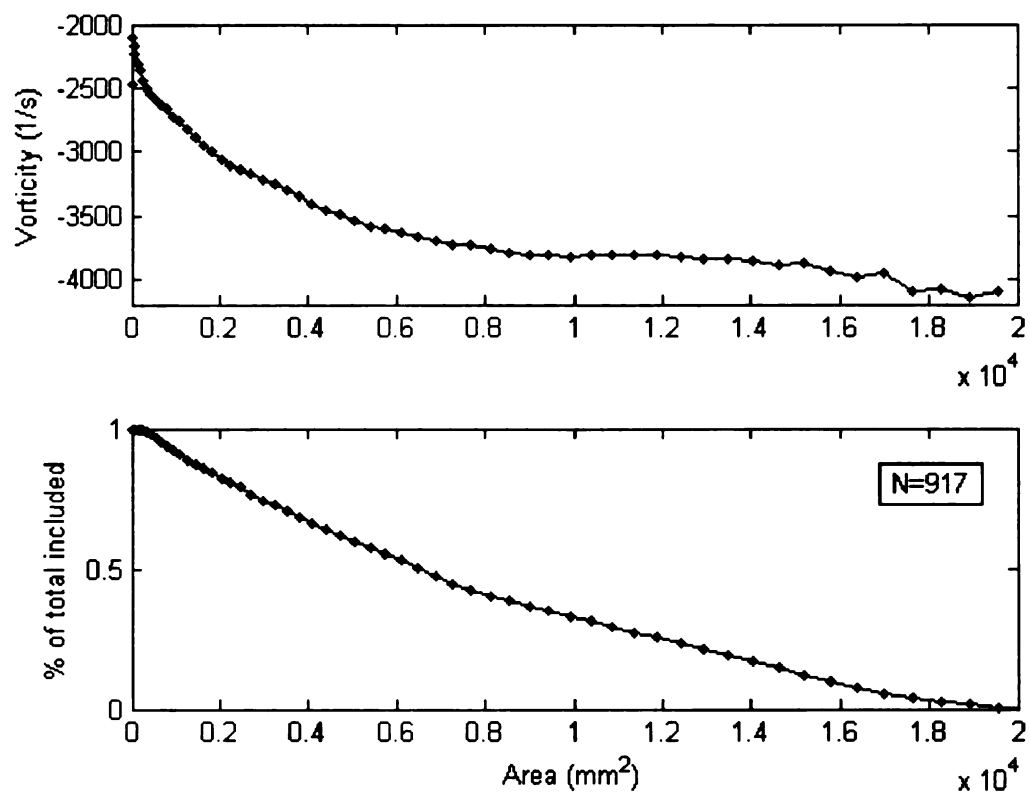
Figure 6.12 Mean Vorticity vs. Area & Samples vs. Area

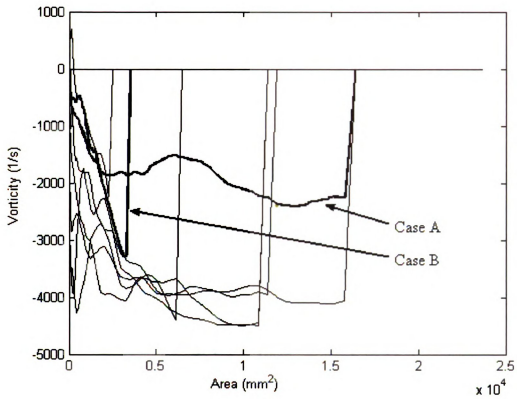**Figure 6.13 Large Scale Node Centered Near the Data Range Border**

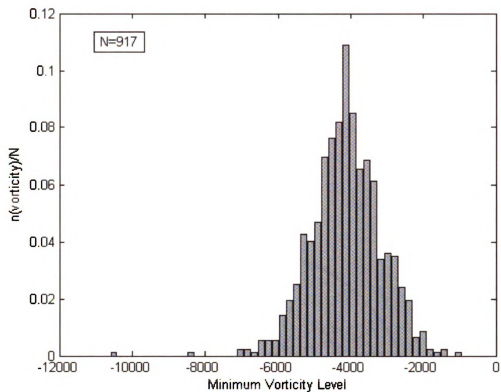**Figure 6.14 Vorticity vs. Area for 10 Individual Nodes**

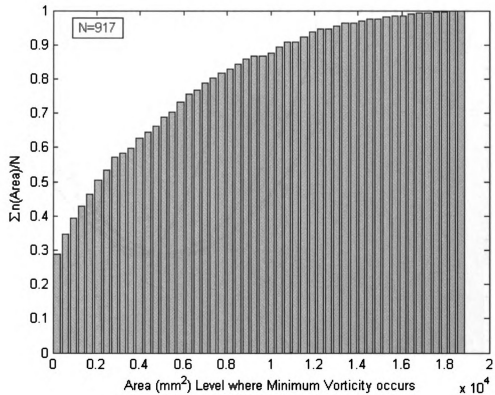**Figure 6.15 Distribution of Minimum Vorticity Level**

Figure 6.16 Cumulative Distribution of the Area at which the Minimum Vorticity Level Occurs
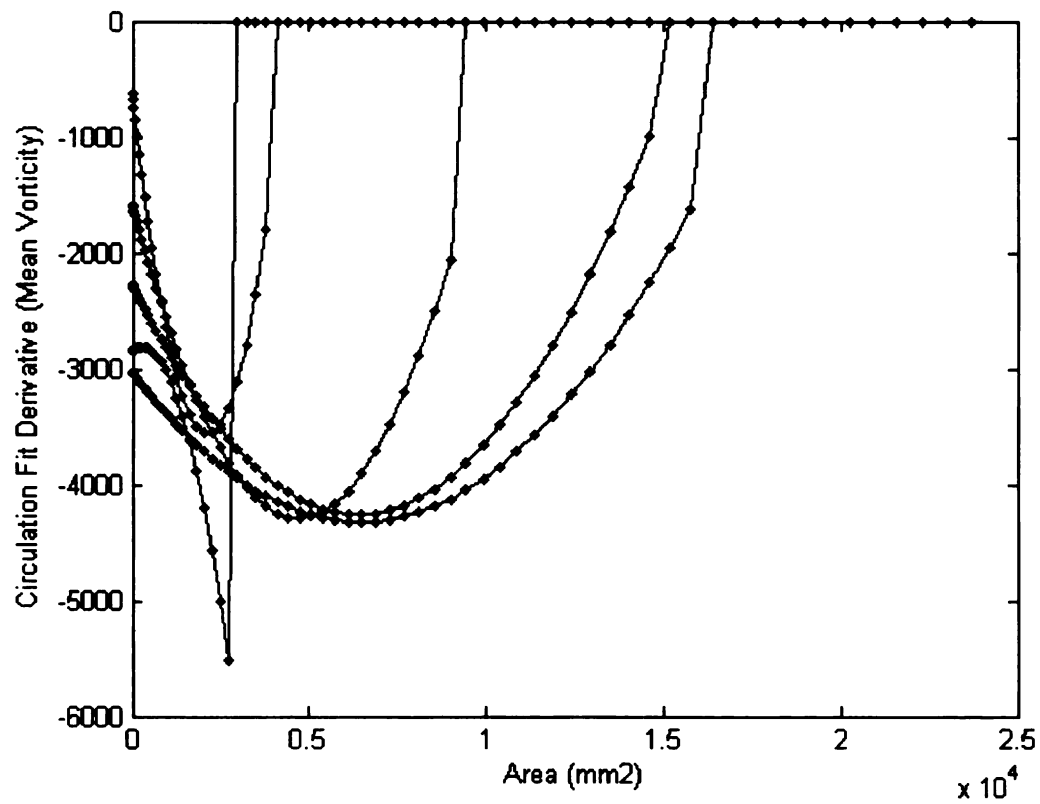
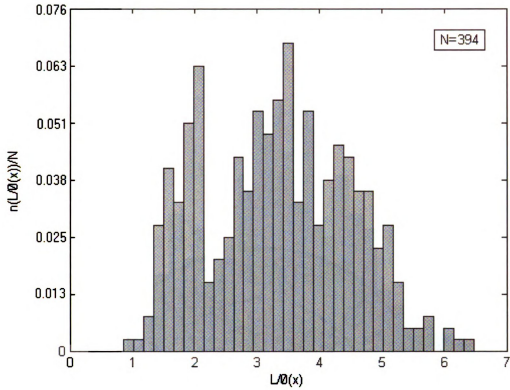**Figure 6.17 Representative Circulation-Derivative (Mean Vorticity) vs. Circulation Contour Area Traces**

Figure 6.18 Distribution of the Normalized Circulation Contour Size where the Mean Vorticity reaches a constant level
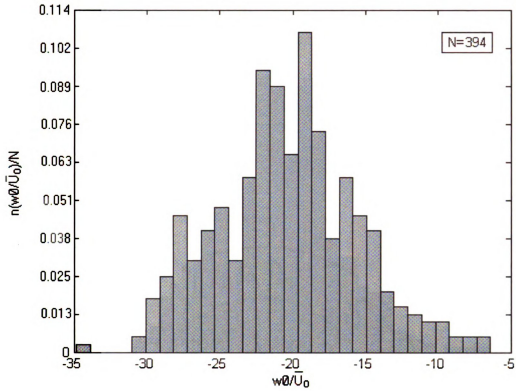
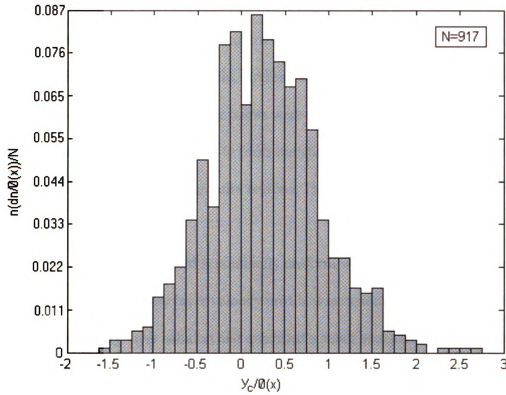**Figure 6.19 Distribution of the Maximum Normalized Strength of Vorticity which becomes Constant**

Figure 6.20 Normalized Distance from Node Circulation Contour Center to the Mean 0.5U_o Isotach

7.0 Summary and Conclusions

A detailed experimental investigation of a shear layer using PIV techniques has been conducted. Detailed data were acquired across the inlet of a backstep test section to assess the details of the inlet flow field. Additional PIV data were acquired to characterize the downstream shear layer. Singular points were identified in the instantaneous downstream PIV images. They were used to form statistical characterizations of the locations, sizes, and strengths of the singular point regions. The following items represent the important results.

1. The inlet velocity field is nominally uniform with small irregularities in the free stream region. The boundary layer velocity profile was in nominally good agreement with the Blasius boundary layer solution and exhibited a small negative pressure gradient. The mean streamwise velocity was $\overline{U}_{o,x=0} = 4.51$m/s at x = 2mm. The initial momentum thickness was $\theta_o = 1.11$mm. The Reynolds number of this flow based on the initial momentum thickness and the mean free stream velocity is $Re_{\theta_o} = 321$.

2. The downstream data revealed a self-similar single-stream shear layer from $(495)\theta_o$ to $(567)\theta_o$ within the $(0.13)\overline{U}_o$ to $\overline{U}_o$ isotach range. The flow system has a secondary, recirculating flow caused by the spacial constraints within the experimental facility. The growth rate, within the single-stream shear layer range, was $d\theta/dx = 0.032$. This is in agreement with published literature concerning single stream shear layers; see Hussain and Zaman (1985). The complete flow field, including the low speed side of the $(0.13)\overline{U}_o$ isotach, somewhat resembled a two-stream shear layer. This interpretation was based on the reduced growth rate of $d\theta/dx = 0.019$ over this larger domain.

3. The maximum mean streamwise velocity was calculated to be $\overline{U}_0 = 4.6$ m/s. The downstream acceleration, $\overline{U}_{0,x=0} = 4.51$ m/s to $\overline{U}_0 = 4.6$ m/s, is attributed to the global recirculating flow.

4. Singular points exist throughout the entire downstream measurement domain. The sum of their indices (node = +1, saddle = -1) was in agreement with a Euler Characteristic constraint of $\chi_{surface} = 0$ for the associated collapsed sphere with two holes.

5. For the domain described in (2) above, the mean spacing of node-saddle pairs was $\langle \frac{\delta y}{\theta(x)} \rangle = -0.0933$ in the spanwise direction and $\langle \frac{\delta x}{\theta(x)} \rangle = 0.0415$ in the streamwise direction. The observed node occurrences were greatly reduced toward the center of the shear layer with no node centers existing in the y > 0 (isotach $\gtrsim 0.68\overline{U}_0$).

6. Coherent motions, surrounding a distinct node and traveling downstream at the convection speed: $\overline{u}/\overline{U}_0 = 0.565$, reach a maximum size and strength which is related to the shear layer momentum thickness. A total of 917 large-scale coherent motions were located and characterized. The location of these convecting node centers was, relative to the $(0.5)\overline{U}_0$ isotach, on average determined to be $\langle \frac{y_c}{\theta(x)} \rangle = 0.26$ (~$0.66\overline{U}_0$ isotach) and with a standard deviation of 0.64. 43% of the circulation investigations reached a constant value within the measurement domain before encountering a domain edge. The mean normalized circulation contour side length, where constant circulation occurred, was $\langle \frac{L}{\theta(x)} \rangle = 3.34$ with a standard deviation of 1.16. The normalized mean vorticity of nodes which reached a constant circulation was $\langle \frac{\overline{\omega}_z \theta(518\theta_o)}{\overline{U}_o} \rangle = -20.4$.

APPENDIX

APPENDIX A

A.0 Large Single Stream Shear Layer (SSSL) Seeding Efforts

Extensive efforts were made in attempting to adequately seed the low speed side entrainment flow of the large SSSL. This appendix will serve to outline the major efforts which were conducted toward this end. Three primary methods were experimentally tested and proven ineffective in supplying proper seed particle density and distribution for the intended measurements. These three primary methods were: a smokewire/hotwire, an installed seeding plenum, and an adjustable seeding unit.

A.1 Smokewire Seeding Method

The smokewire seeding method was experimentally tested in two forms. First a heated wire was used to vaporize fogging fluid which was then carried with the entrainment flow; see Figure A.1. The second form employed the same heated wire to burn a smoke stick. For the first investigation, a thin (D=0.007mm) tungsten wire was wound across 2 supports, located 50cm apart, and stretched taut. The Reynolds number around this wire was much less than 40 which ensured no downstream vortex shedding from the smokewire. The effective Reynolds number around this wire was Re=0.11, based on the flow velocity (V = 0.245 m/s) and the wire diameter. A thin layer of fogging fluid was applied to the wire and an electrical current was supplied in order to heat the wire and vaporize the fogging fluid. This method worked well but did not supply a continuous seed to the flow. This method did however supply a low-density, instantaneous 'line' of seed which could prove useful in an alternative application.

The second smokewire method utilized smoke sticks (incense sticks) which were burned using the heated wire. The smoke sticks were initially reduced in diameter in order to ensure that no vortex shedding would occur on the downstream side of the smoke sticks, this was accomplished by lightly sanding the smoke sticks with a low gauge sandpaper. In order to keep the Reynolds number below 40, with the low speed side entrainment flow velocity of V=0.245m/s, the diameter of the smoke sticks was reduced to less than D=2.5mm. The reduced diameter smoke sticks were then tightly wound with tungsten wire; approximately two revolutions per smoke stick was used. An electric current was then applied and the heated wire caused the smoke sticks to ignite. This supplied a continuous sheet of seed particulate for approximately 30 seconds. One major problem with this method was with the inherently heated smoke particulate matter. Due to the very low flow speed in this region, the buoyancy of the smoke carried the smoke vertically about one-quarter as fast as it was convected towards the shear layer. In other words, for every meter towards the shear layer the smoke traveled, it traveled approximately one-fourth of a meter out-of-plane in the positive z-direction. Additionally, the smoke sheet supplied by the smoke stick was not simply two-dimensional. The smoke which was burned off the smoke sticks was not burned evenly, and therefore the smoke sheet had very pronounced non-uniform density as well as 'waves' in the sheet. There was a negligible likelihood that this sheet would pass precisely and uniformly through the PIV image plane. However, this method provided a sheet of seeded flow which, in a slightly stronger passing flow field, could provide a fairly clean sheet of seed particulate matter for planer observations.

A.2 Installed Seeding Plenum

The installed seeding plenum was the most elaborate of the methods which were attempted. Figure A.2 provides a demonstration of the proposed setup for this method. By intent, this large suspended plenum would be allowed to fill with seeding fluid, then the vertical walls would be dropped and the large volume of seeded fluid within the seeding plenum would convect as part of the entrainment flow. Thin steel cables were stretched, very tightly, across the length of the large single stream shear layer facility. These cables were then used to support a thin sheet of material called 'Monokote'. Monokote is a thin plastic which constricts when heated. The Monokote sheets were designed to make up the horizontal (x-y plane) walls of the seeded plenum. The monokote would then be heated to create a tight, flat, horizontal plenum wall which would only minimally influence the entrainment flow. In practice the light weight Monokote was not able to stretch tight enough to be nominally two-dimensional and therefore this method was abandoned.

A.3 Adjustable Seeding Unit

The adjustable seeding unit (ASU) provided a removable, tunable seeding mechanism which worked moderately well. This unit was, essentially, a small version of the large SSSL's entrainment system. However, unlike the large SSSL the ASU has the capability for seed to pass through it's flow conditioning screens. Figure A.3 provides a schematic of this unit. Figure A.4 supplies a picture of the installed unit in the process of seeding the large SSSL low speed entrainment flow, the seed particulate is illuminated by the PIV laser in this image. By design, this unit would ingest entrainment flow to offset the blockage it presents, then add seed to the flow within the seeding plenum, and finally digest a seeded flow. Minimal disruption to the external flow which was not ingested was

104

the goal. In practice this was accomplished by tuning the inlet fans to ingest the proper amount of flow in order to match the momentum of the external (unseeded) flow. Figure A.5 supplies a plot of the supplied fan voltage versus flow velocity exiting the seeding unit. According to this linear fit, the ideal fan voltage was 6.22 volts in order to match the entrainment flow speed of 0.245m/s. However, even after tuning the inlet fans to this level and other levels, the exiting flow became unstable and coherent motions were observed. These coherent motions could be seen to rotate clockwise or counterclockwise depending on the speed of the inlet fans. Figures A.6-A.8 provide representative images of the flow field with clockwise (positive), counterclockwise (negative), and nearly stable (neutral) motions near the exit of the seeding unit in the y-z plane. The least disruptive level of inlet fan speed was determined and investigated further, however, this method proved insufficient for the intended PIV measurements. Specifically, the seeded entrainment flow possessed a level of disturbance that precluded the desired vortical/non-vortical discrimination method to define the intermittency states: I=1 and I=0 respectively.
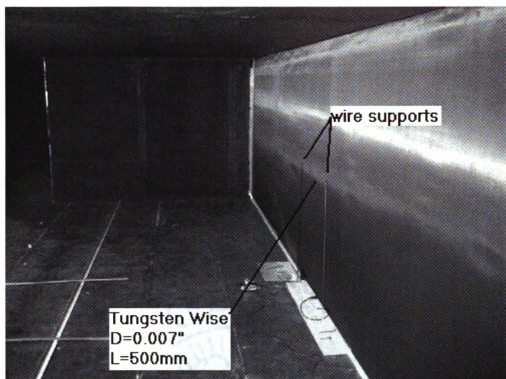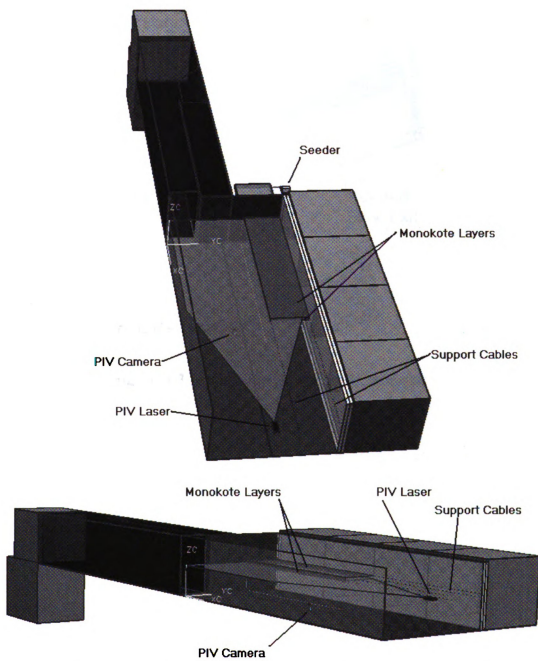
Figure A.1 Installed Smokewire Seeder Prototype

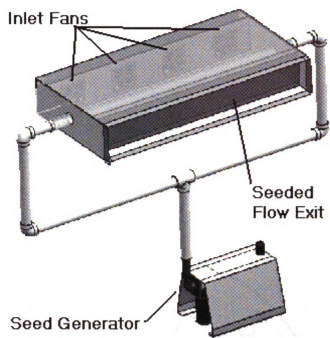**Figure A.2 Large Single Stream Shear Layer with Installed Seeding Plenum**

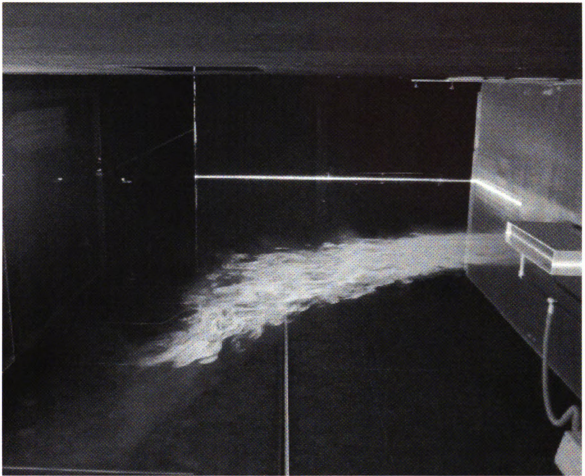**Figure A.3 Adjustable Seeder Unit Schematic**

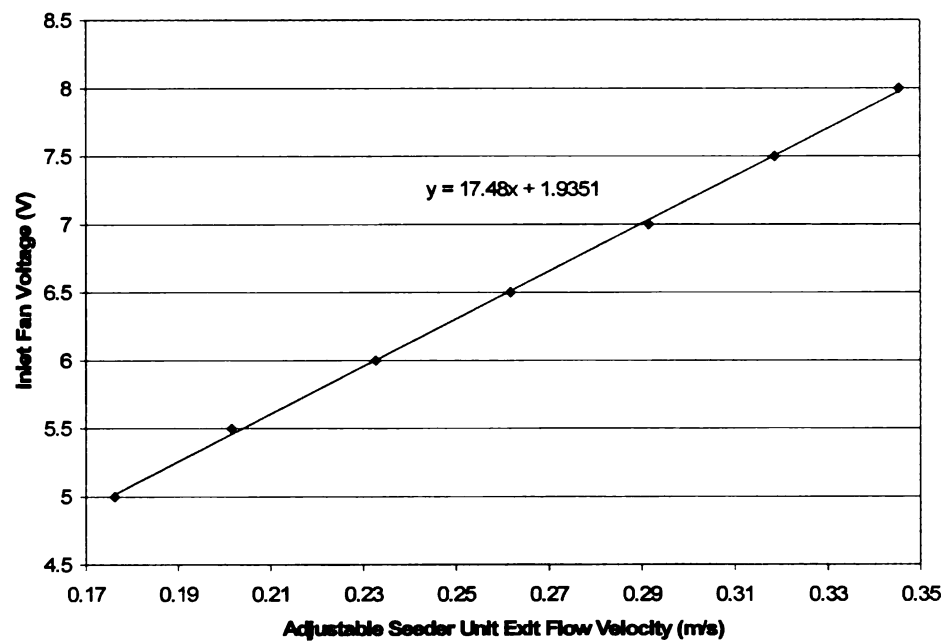**Figure A.4 Installed Adjustable Seeder Unit seeding the large SSSL low speed entrainment flow**

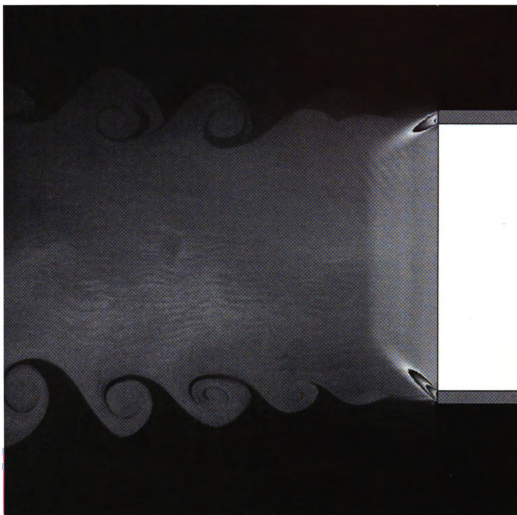**Figure A.5 Inlet Fan Voltage versus Exit Flow Velocity**

Figure A.6 Adjustable Seeder Unit - Positively Tuned (higher seeder exit velocity than external flow velocity)
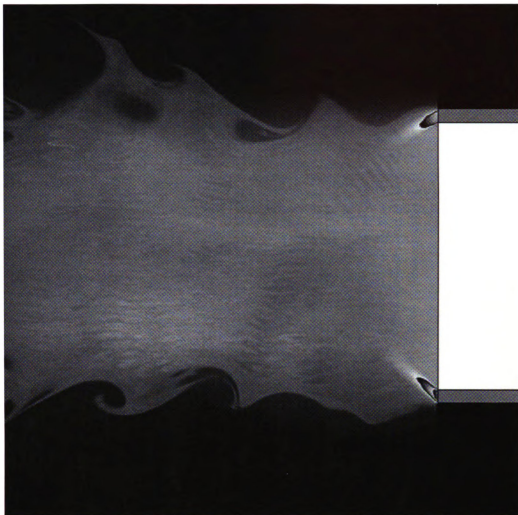
Figure A.7 Adjustable Seeder Unit - Negatively Tuned (lower seeder exit velocity than external flow velocity)
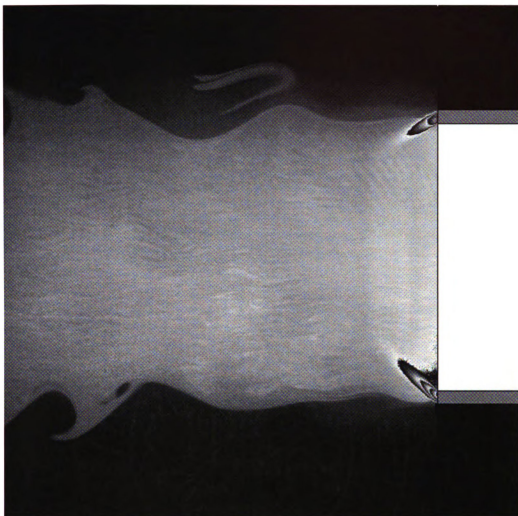
Figure A.8 Adjustable Seeder Unit - Neutrally Tuned (approximately equal seeder exit velocity and external flow velocity)

REFERENCES

REFERENCES

Dimotakis, P.E, (1986), "Two-Dimensional Shear Layer Entrainment," AIAA J. **24**, 1791-1796.

Foss, J.F., (2004), "Surface selections and topological constraint evaluations for flow field analyses," Experiments in Fluids, vol. 37, pp. 883-898.

Foss, J.F., (2007), Handbook of Experimental Fluid Mechanics, Ed C. Tropea, J Foss, A Yarin, Springer Verlag.

Hellum, A.M., (2006), "Intermittency and the Viscous Superlayer in a Single Stream Shear Layer," M.S. Thesis, Department of Mechanical Engineering, Michigan State University, East Lansing, MI.

Hussain, A.K.M.F. & Zaman, K.B.M.Q., (1985), "An experimental study of organized motions in the turbulent plane mixing layer.", *J. Fluid Mech.*, vol. 159, pp. 85-104.

Jones, B.G., Hammersley, R.J., Planchon Jr., H.P., and Spencer, B.W., "The Turbulence Structure in the Plane Two-Stream Mixing Layer," Nuclear Engineering Program, University of Illinois at Urbana-Champaign, (Report).

LaVision GmbH., (2002), *FlowMaster Manual*, Gottingen, Germany, p. 50-67.

Liepmann, H.W., & Laufer, J. (1947), "Investigation of free turbulent mixing". *N.A.C.A. Tech. Note*, no. 1257.

Morris, S.C., (2002), "The Velocity and Vorticity Fields of a Single Stream Shear Layer," Ph.D. Dissertation, Department of Mechanical Engineering, Michigan State University, East Lansing, MI.

Morris, S.C., Foss, J.F., (2003), "Turbulent boundary layer to single-stream shear layer: the transition region," J. Fluid Mech., vol. 494, pp. 187-221.

Perry, A.E. and Chong, M.S., (1987), "A description of eddying motions and flow patterns using critical-point concepts," Annu. Rev. Fluid Mech, 19:125-155.

Spencer. B.W., (1970), "Statistical Investigation of Turbulent Velocity and Pressure Fields in a Two-Stream Mixing Layer," Ph.D. Thesis, Nuclear Engineering Program, University of Illinios.

Winant, C.D. and Browand, F.K., (1974), "Vortex Pairing: The Mechanism of Turbulent Mixing Layer Growth at Moderate Reynolds Number," Journal of Fluid Mechanics, Vol. 63, Part 2, pp. 237-255.

Wignanski, I. and Fiedler, H.E., (1970), "The Two-Dimensional Mixing Region," *Journal of Fluid Mechanics*, vol. 41, pp. 327-361.